# A Computational Study on Spiral Blood Flow in Stenosed Arteries with and without an Upstream Curved Section

M. A. Hye[1,2] and M. C. Paul[1] *

[1]School of Engineering, University of Glasgow,

Glasgow G12 8QQ, UK

[2]Department of Mathematics,

Shahjalal University of Science and Technology,

Sylhet 3114, Bangladesh

**Abstract**

Spiral and non-spiral blood flows through three-dimensional models of 75% axisymmetric arterial stenosis are investigated by using two-equation standard $k$-$\omega$ transitional model and Large Eddy Simulation (LES). The arterial stenosis models chosen are straight stenosed tubes without and with upstream curved segments of various angles of curvature. The Reynolds numbers investigated are 500, 1000, 1500 and 2000. Spiral effect is introduced by taking one-sixth of the bulk velocity as a tangential velocity at the inlet, and the inlet turbulence intensity was introduced for matching experimental results. LES results with a right amount of inlet turbulence intensity matches experimental results better than the $k$-$\omega$ results. The results show that the spiral flow affects the turbulence kinetic energy in the post stenosis region. Other

*Email: Manosh.Paul@glasgow.ac.uk, Tel:+44 (0)141 330 8466

important results such as the wall pressure and shear stress remain almost unchanged by the spiral velocity. But the presence of the upstream curved segment in artery moderately affects the results of the maximum pressure drop and wall shear stress.

Keywords: Arterial stenosis, Non-spiral flow, Spiral flow, Transition-to-turbulence flow, $k$-$\omega$, LES

# 1 Introduction

An interesting feature of blood-flow is its spiral or helical characteristic. Blood-flow may exhibit spiral pattern as a normal physiological process i.e., because of the twisting of the heart on its own axis and/or because of the anatomy of the arterial tree such as the presence of bifurcation, tapered or curved section in an artery (see Stonebridge [1], Stonebridge et al. [2]). The hemodynamics of stenosed artery in the downstream of stenosis is significantly altered when non-spiral or spiral blood flow passes through the stenosis depending on the degree of stenosis and inflow pattern, resulting in potentially dangerous pathological scenarios. The post-stenotic flow is highly disturbed due to the flow passing through moderate or severe stenosis and transients to turbulence state. With the state-of-the-art computing facilities, numerous studies have been carried out to get a sound understanding of transition-to-turbulence phenomena of non-spiral flow through stenosis. However, to get a better insight into the transition-to- turbulence flow through the arterial stenosis, spiral effect should be incorporated into the flow. But computational studies on spiral blood flow through stenosis are very few and incomplete.

Stonebridge et al. [3] and Paul and Larman [4] investigated spiral blood flow through stenosis and carried out turbulence analysis of the flow in stenosed artery. Stonebridge et al. [3] investigated steady spiral flow in moderately stenosed (43.75% area reduction) conduit using MRI and CFD software STAR-CD.

On the other hand, Paul and Larman [4] studied steady spiral blood flow through a rigid stenosed pipe with 75% area reduction stenosis for Reynolds number of 500 and 1000 using $k$-$\omega$ model and showed most of the results including the turbulence kinetic energy along the centreline. They found the spiral flow generates less turbulence kinetic energy (TKE) than the non-spiral flow for $Re = 500$ and no difference between the spiral flow TKE and the non-spiral flow TKE for $Re = 1000$. But, maximum turbulence intensities occur in the shear layer rather than along the centreline (Deshpande and Giddens [5]). Moreover, their other results (centreline total pressure and wall shear stresses) show that differences between spiral and non-

spiral flow exist mostly for $Re = 500$, not for $Re = 1000$. Apart from the twisting of the heart on its own axis, spiral pattern in blood flow may also be generated due to the presence of a curved section in the upstream. Above mentioned two studies were only on a straight stenosed tube. Therefore, to get a better insight of the transition-to-turbulence of spiral blood flow through arterial stenosis, more numerical investigations are required.

In this paper, transition of steady spiral blood flow through models of arterial stenosis with and without an upstream curved section is studied by applying two-equation standard $k$-$\omega$ transitional turbulence model and LES technique. The $k$-$\omega$ turbulence model was previously used by other researchers (e.g. see Ghalichi et al. [6], Varghese and Frankel [7], Lee et al. [8, 9] and Li et al. [10]) to study the axisymmetric stenotic flow. In the context of LES applications, most recent studies include Varghese et al. [11], Paul et al. [12, 13, 14, 15], Tan et al. [16], Gårdhagen et al. [17] and Barber and Simmons [18].

Straight tubes having axisymmetric stenosis with and without upstream curved segment of varying angles are taken as the computational domains. A parabolic profile for axial velocity was introduced at the inlet. And for generating spiral effect at the inlet, one-sixth of the bulk velocity was taken as the tangential velocity, as suggested by Stonebridge et al. [2, 3] that the spiral velocity is one-sixth of the forward velocity within the artery. At the outlet, a constant static pressure of 80 mmHg (or 10665.6 Pa) was imposed. In this study, the focus is on the effects of spiral pattern on the flow physics in the downstream region of the stenosis.

The filtering operation in LES divides the flow field up into large scale eddies and small scale (Sub-grid scale or SGS) eddies. The turbulence energy containing large scale eddies are resolved directly while the unresolved small scale eddies are modelled using Smagorinsky-Lilly dynamic subgrid model (Germano [19], Lilly [20] and Kim [21]). The commercial code Fluent 6.3 is validated for axial velocity profiles in the non-spiral blood flow in a model arterial stenosis for Reynolds numbers $Re =$ 1000 and 2000 against available corresponding experimental data of Ahmed and

Giddens [22, 23]. The performance of $k$-$\omega$-$SST$ transitional model in comparison with standard $k$-$\omega$ transitional model is also assessed by comparing the axial velocity profiles obtained from using them against the available corresponding experimental data. In addition, it is also examined how much inlet turbulence intensity can be introduced in LES and $k$-$\omega$ transitional model to control transition and hence benchmark against the experimental data. Effects of spiral pattern on the post-stenotic flow are assessed in terms of some important turbulence results such as the turbulence kinetic energy, wall shear stress and wall pressure along with their relevant pathophysiological implications.

# 2 Problem formulation

## 2.1 Flow Models and Meshing

Solid models of stenosed arteries with and without upstream curved section of varying angles were built using GAMBIT 2.4 (Fluent Inc.) and are shown in Fig. 1. Diameter of the unstenosed section of the arterial models is $D = 0.02m$ and the angle of curvature ($\theta$) for the upstream curved sections are: 60°, 90° and 120°. Axial direction is along the $z$-coordinate axis. For the straight tube (without upstream curved section), stenosis is centred at $z = 0$. Length of the stenosis, upstream and downstream sections of the model arteries are $2D$, $3D$ and $22D$ respectively, as measured from the stenosis throat. Vessels with curved upstream section are further extended to $10D$ in the upstream as shown in Fig. 1. Degree of a stenosis is generally measured by a percentage reduction in diameter or cross-sectional area at the throat of the stenosis. For our study a 75% stenosis by area reduction, corresponding to a 50% diameter reduction was used as it is clinically significant when the area reduction is greater than 75% (Young [24] and Ku [25]). Furthermore, a 75% stenosis has also been used in many previous experimental and computational studies.

The stenosis is formed using the following cosine-type relation

$$\frac{r\left(z\right)}{R} = 1 - \frac{\delta_c}{2}\left(1 + \cos\frac{z\pi}{D}\right), \quad -D \leq z \leq D \tag{1}$$

where $r$ and $R$ are the local radius (radial co-ordinate) and radius of the models respectively. The parameter $\delta_c$ determines the cross-sectional area reduction of the stenosis and it is fixed to $\frac{1}{2}$, giving a 75% reduction of the cross-sectional area at the centre of the stenosis. The cosine-type realistically shaped constriction/stenosis developed in the model arteries using the above relation (1) provides a quite reasonable representation of an arterial stenosis, see Ahmed and Giddens [23].

Meshing of the flow domains was done using the meshing software GAMBIT 2.4 (Fluent Inc.). As no-slip condition is applied to the wall, a boundary layer is developed inside the wall to increase the resolution in the sublayer. A gradient scheme is also applied along the axial direction of the models to ensure the finest mesh at the centre and immediate downstream of the stenosis because high level of vortices and turbulence fluctuations occur in these regions. And in the further downstream region of the stenosis a gradually coarsening mesh helps keeping computational cost to a minimal.

## 2.2 Governing Equations

Blood exhibits non-Newtonian effects only in small arteries and capillaries. Hence, blood flow in a large arterial vessel may be modelled as a Newtonian fluid (Ku [25], Pedley [26] and Fung [27]). So the blood flow through the arterial stenosis can be described completely by the Navier-Stokes equations of motion. Blood in this study was assumed to be homogeneous, incompressible and Newtonian with a density of $\rho = 1060$ kg/m$^3$ and a constant dynamic viscosity of $\mu = 3.71 \times 10^{-3}$ Pa s. Therefore, the governing equations for a Newtonian and constant density blood flow can be written as the continuity equation,

$$\frac{\partial u_i}{\partial x_i} = 0, \tag{2}$$

and the momentum equations,

$$\frac{\partial u_i}{\partial t} + \frac{\partial u_i u_j}{\partial x_j} = -\frac{1}{\rho}\frac{\partial p}{\partial x_i} + \frac{\partial}{\partial x_j}\Big[\nu\left(\frac{\partial u_i}{\partial x_j} + \frac{\partial u_j}{\partial x_i}\right)\Big]. \tag{3}$$

Cartesian tensor notation is used in the above equations, where $x_i$ is the coordinate system and $u_i$ is the corresponding velocity components, $p$ is the pressure, $\rho$ is the density and $\nu$ is the kinematic viscosity of fluid.

It should be noted that the above equations define both incompressible laminar and turbulence flow. Analytical solutions of the Navier-Stokes equations exist for only a few laminar flow cases, such as pipe and annulus flows or boundary layers. Turbulence flows are modelled by using various turbulence modelling schemes. In this study, two-equation $k$-$\omega$ Transitional models and LES are employed for turbulence analysis.

## 2.3 Inflow Boundary Condition

A parabolic velocity profile along the axial direction:

$$w(x,y) = 2\bar{V}\Big[1 - \left(\frac{r}{R}\right)^2\Big], \tag{4}$$

where $\bar{V}$ is the bulk axial velocity which depends on the blood flow Reynolds number defined as $Re = \frac{\rho \bar{V} D}{\mu}$, is imposed at the inlet of the models. And for introducing the spiral flow, a tangential velocity profile defined as

$$v_t = \frac{\bar{V}}{6}\left(\frac{r}{R}\right), \tag{5}$$

is applied at the inlet. These inlet boundary conditions were coded in C-language using the User Defined Function (UDF) interface of Fluent and linked with the solver. In this paper, each model is investigated for four Reynolds numbers namely $Re$ = 500, 1000, 1500 and 2000. The parameters of the models are presented in Table 1 and models will be referred by their names in the following sections of the paper.

Inlet turbulence characteristics are defined by inlet turbulence intensities and diameter of the model. For the $k$-$\omega$ models, inlet turbulence intensity of 3.8%,

Table 1: Parameters of stenosed arteries with and without upstream curved section models.

| Model | $\theta$ (angle of curvature) | $Re$ |
|---|---|---|
| $A1$ | 0° | 500 |
| $A2$ | 60° | 500 |
| $A3$ | 90° | 500 |
| $A4$ | 120° | 500 |
| $B1$ | 0° | 1000 |
| $B2$ | 60° | 1000 |
| $B3$ | 90° | 1000 |
| $B4$ | 120° | 1000 |
| $C1$ | 0° | 1500 |
| $C2$ | 60° | 1500 |
| $C3$ | 90° | 1500 |
| $C4$ | 120° | 1500 |
| $D1$ | 0° | 2000 |
| $D2$ | 60° | 2000 |
| $D3$ | 90° | 2000 |
| $D4$ | 120° | 2000 |

1.5%, 1.0% and 0.7% is found to give acceptable results for $Re$ = 500, 1000, 1500 and 2000 , respectively , as it is clear from the experimental validation for two Reynolds numbers presented in § 4. LES is applied to only model $D1$ for both the non-spiral and spiral blood flow cases and model $B1$ for the non-spiral blood flow. Three different inlet turbulence intensities: 0% i.e., no inlet perturbation, 1% and 5% are considered for experimental validation. The inlet perturbations in LES were generated using the vortex method ([28]) and the magnitude of these artificial intensities adjust downstream from the inlet. A time-step size of $1.0 \times 10^{-3}$ s is taken for temporal advancement in LES. Instantaneous axial velocity at several points on the centreline is recorded for each time-step and sampling for time statistics is initiated when the initial transients has vanished. A total time-steps of 15000 are used to get statistical convergence when the time averaged values have levelled off. Results presented in the paper are mainly of $k$-$\omega$ model unless it is mentioned otherwise.

# 3 Overview of Numerical Procedures

An outline of the solution procedure used this study is laid out in this section. The cell-centered finite volume fully implicit and second order accurate in both space and time code, Fluent 6.3, with its turbulence models namely two-equation $k$-$\omega$ Transitional model and LES with Smagorinsky-Lilly dynamic subgrid model was employed to solve the incompressible governing equations for the spiral blood flow through the models of arterial stenosis. Fluent with above mentioned turbulence models has previously been exploited to investigate pulsatile and steady flow in arterial stenosis by Ryval et al. [29], Varghese et al. [11], Paul and Larman [4], Barber and Simmons [18] and Gårdhagen et al. [17].

Pressure-based fully implicit solver was chosen for this study. Finite-volume approach is used to discretise the governing equations to construct a system of linear equations. For the $k$-$\omega$ Transitional model, the diffusive and convective terms

of the momentum equations and the equations of turbulence kinetic energy ($k$) and specific dissipation rate ($\omega$) were discretised by using second-order upwind scheme. However, in LES, a second-order-accurate bounded central differencing scheme is used to discretise the diffusive and convective terms of the momentum equations. And the pressure at a cell face was computed using second-order scheme for both LES and $k$-$\omega$ Transitional model. In addition, three-point backward difference scheme is used to discretise time derivatives.

A segregated pressure correction algorithm, SIMPLEC (Vandoormaal and Raithby [30]) for the $k$-$\omega$ Transitional model and PISO (Pressure-Implicit with Splitting of Operators, Issa [31]) for LES, is employed to couple pressure with the velocity components and results are stored at the cell centres as the code uses a co-located scheme. To prevent unphysical checker-boarding of pressure, the Poisson like pressure-correction equation is discretised by using a procedure similar to Rhie and Chow [32] pressure smoothing approach. The pressure correction equation is solved by using the algebraic multigrid (AMG) method. Splitting error, introduced by segregated solution process, is controlled by using an iterative-time advancement scheme.

A point implicit (Gauss-Seidel) solver in conjunction with algebraic multigrid (AMG) method is used to solve the discretised system of linear equations. For all the computations, convergence is assumed to have achieved when the residuals become less than 1, normalised by$10^{-5}$.

# 4 Validation with Experiment

Before discussing the main results, it would be interesting to see how the simulation results obtained from using the different turbulence models match the available experimental results of Ahmed and Giddens [23, 22]. Figs. 2 and 3 show a comparison of the axial velocity profiles at various locations downstream of the stenosis models $B1$ and $D1$ respectively for the non-spiral flow i.e., straight tube with 75% cross-sectional area reduction stenosis for the Reynolds numbers $Re = 1000$ and

2000 respectively. Velocity profiles in models $B1$ and $D1$ obtained by using the $k$-$\omega$ models with an inlet intensity of 1.5% and 0.7% respectively closely follow the corresponding experimental data, though they over-predict in the further downstream region. For the $k$-$\omega$ models, any inlet intensity lower than the above intensities for a corresponding geometric model gives unconvincing velocity profiles as it is clear from Figs. 2 and 3. It is to note from the above figures that the standard $k$-$\omega$ (skw) transitional and $k$-$\omega$-$SST$ transitional models give almost the same results, i.e., none of the two $k$-$\omega$ models matches the experimental data better than the other. So, the standard $k$-$\omega$ transitional model will be used in preference to the $k$-$\omega$-$SST$ transitional model.

Three distinct inlet perturbations, 0%, 1% and 5% were introduced in LES for both geometric models $B1$ and $D1$. It appears from the above figures that the LES with a 0% inlet intensity agrees better with the experimental results than the other two inlet intensities for model $B1$. However, for model $D1$, the LES with a 5% inlet intensity matches the experimental data better. Therefore for model $D1$, 5% inlet intensity will be used in this study. Furthermore, performance of LES is obviously better than the $k$-$\omega$ transitional model as it can be seen that the blunt turbulence velocity profiles in the downstream region from the experimental data matches only the LES results. In spite of small disagreements with the experimental results of Ahmed and Giddens [23, 22], which are also present in the studies of Ryval et al. [29] and Gårdhagen et al. [17], overall agreement of the present simulation results with the experimental results is very good.

# 5 Results and discussion

Although all the geometric models are studied for the spiral blood flow, results from models $D1$, $D2$, $D3$ and $D4$ are presented in detail while the findings from all the models are summarised in bar charts at the end. As the focus is on the effects of spiral pattern on the flow field in the downstream of the stenosis, results in the

curved section of all the models having upstream section are ignored to compare the results in the remaining section with corresponding results in the stenosed straight tube without upstream curved section.

## 5.1 Grid Resolution Study

Grid resolution tests are done for the spiral flow in two models namely $D1$ and $D3$ by applying the LES and standard $k$-$\omega$ transitional model respectively to ensure simulation results are independent of grid arrangements employed. The test results are shown in Figs. 4 and 5 for the axial velocity profiles at different locations along the axial directions. In Fig 4 for model $D1$, Grid 1 corresponds to a total of $\approx 500,000$ control volumes which is increased by 40% for Grid 2 to get $\approx 700,000$ control volumes. Grid 3 consists of huge control volumes i.e., $\approx 1,260,000$ which is further 80% increase of Grid 2. However, in Fig 5 for model $D3$, Grid 1, Grid 2 and Grid 3 consists of $\approx 750,000$ , $950,000$ and $1,500,000$ control volumes respectively, keeping almost the same ratio of control volumes as in model $D1$. The grid resolution studies in Figs. 4 and 5 clearly show that resolution of Grid 2 is good enough to get high level accuracy in the simulation while keeping the computational cost to a minimum. In addition, three different time-step ($dt = 1.5 \times 10^{-3}s$, $1.0 \times 10^{-3}s$ and $8.5 \times 10^{-4}s$) were used and the results obtained with $dt = 1.0 \times 10^{-3}s$ showed to have a good time-step independency.

## 5.2 Assessment of Flow Field

To see how the flow field in the downstream of the stenosis in the non-spiral flow differs from that of the spiral flow, cross-sectional streamlines are appended on the contour plot of the axial velocity at various locations along the flow directions in Figs. 6-9 for models $D1$ and $D3$. Fig. 6 demonstrates that the re-circulation region, evidenced by the presence of the negative axial velocity near the walls, for the non-spiral flow in model $D1$ is between $2D$ (frame e) and $4D$ (frame g). While for the spiral flow in the same model, the re-circulation region is predicted to be slightly

larger and lies between $2D$ (frame e) and $5D$ (frame h), as seen in Fig. 7. Also the twisting pattern of the spiral flow in this region is much stronger and the spiral property tries to stabilise the flow towards the the further downstream region. The large recirculation zones in the downstream of model stenosis are clinically harmful as these may cause potential damage to blood cells and intima of the stenosed artery (Paul and Larman [4], Paul et al. [12]).

The "twisted" pattern found in the downstream of the spiral flow in model $D1$, as seen in Fig. 7, is similar to the "corkscrew" pattern found in the MRI measurements of the blood flow in a thrombosed artery by Frydrychowicz et al. [33]. However, the length of the recirculation zone for the non-spiral and spiral flow in model $D3$ is almost same and lies between $2D$ (frame e) and $5D$ (frame h), as it is clear from Figs. 8 and 9. Further, it is to note that unlike the spiral flow in model $D1$ as in Fig. 7, no stable spiral pattern is seen in the upstream region and at the throat of the stenosis for either non-spiral or spiral flow in model $D3$. But for the spiral flow in model $D3$ as in Fig. 9, a rotational pattern is visible in the further downstream region. Moreover, two distinct recirculations of secondary flow can be observed for both non-spiral and spiral flow in model $D3$ at $-3D$ (frame a) in the upstream of the stenosis due to the presence of a curved section. Additionally, for both spiral and non-spiral flow in models $D1$ and $D3$, velocity vectors move towards the centre at the throat of the stenosis where the axial velocity is maximum. At the onset of turbulence at $2D$ (frame e), direction of the vectors reverses from their previous direction at $1D$ (frame d) where they start to break away from the centre as it is clear from Figs. 6, 7, 8 and 9.

The mean axial velocity, $\langle w \rangle$, profiles for both the non-spiral and spiral flow at different locations in the models $D1$ and $D2$, $D3$ and $D4$ are presented in Figures 10 and 11, respectively. Note that the corresponding LES results in model $D1$ are also appended in Figure 10. As blood enters the stenosis, it accelerates through the constriction, generating a plug-shaped velocity profile within the stenosis and a flow separation region immediately downstream of the stenosis. No substantial effect of

the spiral flow on the axial velocity is observed from the above figures. However, the axial velocity in model $D1$ increases for the spiral flow near the wall and decreases around the centre between $2D$ (frame d) and $4D$ (frame f) which can be seen from the LES results. In the further downstream region, i.e. after $8D$ (frame j), it is almost same for all the models. But the magnitude of the axial velocity around the centre is maximum in model $D1$ in the immediate downstream region and it falls slightly from this maximum value in model $D3$. While it is minimum in models $D2$ and $D4$. Particularly, it is found that the axial velocity decreases in model $D4$ compared to that of $D2$ around the mid-region between the wall and the centre in the downstream between $3D$ (frame e) and $4D$ (frame f). All these differences in the axial velocity profiles in the different models are due to the effect of an upstream curved segment of varying angles of curvature.

Figures 12 and 13 show the mean $x$-velocity (radial), $\langle u \rangle$, profiles at different locations in models $D1$ and $D2$, $D3$ and $D4$, respectively. The LES results for the mean $x$-velocity differ significantly from the corresponding $k$-$\omega$ model results, which can be seen from Figure 12. Also in model $D1$, the spiral effect on $\langle u \rangle$ is distinctly visible, especially up to $9D$ (frame k) as the $\langle u \rangle$ profiles in the non-spiral flow vary in magnitude and pattern from those in the spiral flow. However, in other models, the effect of the spiral flow is not significant on $\langle u \rangle$, as it is clear from Figure 13. The magnitudes of $\langle u \rangle$ are maximum in model $D2$ and of opposite pattern in model $D4$ which can be attributed to the existence of an upstream curved segment of different angles of curvature.

The mean $y$-velocity (tangential) profiles, $\langle v \rangle$, in models $D1$ and $D2$, $D3$ and $D4$ are shown in Figures 14 and 15, respectively, to see the influence of the spiral flow and an upstream curved section on $\langle v \rangle$. As already seen in the $\langle u \rangle$ profiles, the LES results for $\langle v \rangle$ do not match the corresponding $k$-$\omega$ model results, which is clear from Figure 14. Due to the effect of spiral velocity introduced at the inlet, the $\langle v \rangle$ profiles for the spiral flow at different locations differ from the corresponding results for the non-spiral flow in model $D1$, which can also be seen from this figure,

especially from the LES results. In the other models, as can be seen in Figure 15, the effect of the spiral and upstream curved section on $\langle v \rangle$ is also distinctly visible. Particularly, at some places in the downstream region up to $5D$ (frame g), $\langle v \rangle$ is maximum in model $D4$ which is followed by its corresponding value in models $D3$ and $D2$. In the further downstream region, the $\langle v \rangle$ profiles are almost same in all models.

## 5.3 Turbulence Characteristics

The effects of the spiral flow and upstream curved segment on the turbulence kinetic energy (TKE) at different locations in the flow domain in models $D1$ and $D2$, $D3$ and $D4$ are presented in Figures 16 and 17, respectively. The LES results in Figure 16 clearly show that in model $D1$ at some places between $2D$ (frame d) to $5D$ (frame g) i.e., in the core turbulence region, the TKE increases for the spiral flow though it may decrease along the centreline as shown by Paul and Larman [4]. Also the TKE in model $D2$ increases at some places when a spiral effect is introduced at the inlet of the model as can be seen from Figure 17(d-f). No major influence of the spiral flow on the TKE in the other models ($D3$ and $D4$) can be seen from Figure 17. It remains same at the corresponding locations, however, the TKE is high in the post-stenotic region between $2D$ (frame d) and $6D$ (frame h). The high TKE in the post-stenotic region for the spiral flow in models $D1$ and $D2$ has even more serious detrimental effect on the human circulatory system because large TKE damages the red blood cell materials and activates the platelets in the blood leading to many pathological diseases (Ku [25]).

## 5.4 Wall Pressure and Shear Stress

Circumferential average wall pressure and wall shear stress (WSS) obtained from all the models are presented in Figs. 18 and 19 respectively. Fig. 18 generally shows that the wall pressure drop around the stenosis throat is greater in models $D1$ and $D3$ than that of the other two models $D2$ and $D4$. Particularly, the wall pressure

drop in model $D3$ is maximum and it is same and minimum in models $D2$ and $D4$. The LES results also show that the wall pressure recovers in model $D1$ earlier than the other models after the drop and some variations between the results of spiral and non-spiral flow are found in the downstream region. It should be noted that the high Bernoulli-type pressure drop at the stenosis throat could potentially cause local collapse of the stenosis in severe stenoses (Wootton and Ku [34]). Consequently, choking can restrict the flow rate, and generated compressive loading may rupture the plaque, a precipitating event in most heart attacks and stroke (Wootton and Ku [34], Li et al. [35]).

The WSS increases just prior to the throat of the stenosis in Fig. 19 because of the high velocity found at the throat. It drops just after the throat where it is almost zero and takes an oscillatory form in the post-stenotic region. Like the pressure drop, the WSS increases just before the throat and it is maximum (31 Pa) and almost same in models $D1$ and $D3$. While in models $D2$ and $D4$, the WSS is of same value and prior to the throat it increases (25 Pa) less than that in the other two models. This high increase in WSS just before the throat has many pathological significances. Malek et al. [36] reported that the shear stress higher than 70 dynes/cm$^2$ (or 7 Pa) may induce thrombosis. According to Fry [37], high WSS ($> 379 \pm 85$ (SD) dynes/cm$^2$) around the throat may damage endothelial cells and fissure plaque. And it may also overstimulate platelet thrombosis (Ku [25]), leading to a total occlusion (Folts et al. [38]). Additionally, high shear stress ($>$ 100 dynes/cm$^2$ or 10 Pa) is also responsible for deformation of the red blood cells (Sutera and Mehrjardi [39]). Moreover, the abnormal oscillatory shear stress found in the downstream of the stenosis in all the models may cause potential damage to the red blood cells and the inner lining of a post-stenotic blood vessel (Paul and Molla [15]).

## 5.5 Summary of the other models

Bar charts in Fig. 20 summarise the effects of the spiral flow and upstream curved segments on the maximum (derived from the whole domain) TKE in all the models. The maximum TKE increases slightly for the spiral flow in models $A1$, $B1$, $B3$, $C2$, $D1$ and $D2$; while for the spiral flow in models $A2$, $A3$, $A4$, $B2$, $B4$, $C4$ and $D4$ it decreases a little and its change in the remaining models is very insignificant. Specifically, for the spiral flow, the maximum increase in TKE is $\approx 6\%$, $\approx 2\%$, $\approx 3\%$ and $\approx 5\%$ for $Re = 500$ in the straight stenosed tube, $Re = 1000$ in the straight stenosed tube, $Re = 1500$ in the 60° curved upstream model, and $Re = 2000$ in the 60° curved upstream model, respectively. And the maximum decrease in TKE is $\approx 7\%$, $\approx 3\%$, $\approx 2\%$ and $\approx 2\%$ for $Re = 500$ in the 60° curved upstream model, $Re = 1000$ in the 60° curved upstream model, $Re = 1500$ in the 120° curved upstream model, and $Re = 2000$ in the 120° curved upstream model respectively.

Influence of the upstream curved segment on the maximum TKE can also be seen for all the Reynolds numbers. For example, for the Reynolds numbers $Re = 1000$, 1500 and 2000, the maximum TKE increases most in the model with 120° curved upstream segment which is followed by the maximum TKE in the 60°, 90° and 0° curved upstream segment models respectively. But for $Re = 500$, the maximum TKE decreases most in the 120° curved upstream segment model. In terms of their quantitative comparisons, the maximum TKE rises 18%, 18% and 19% in the 120° curved upstream model from its minimum value in the straight stenosed tube for $Re = 1000$, 1500 and 2000 respectively. While for $Re = 500$, it rises 34% in the 60° curved upstream model from its minimum value in the 120° curved upstream model. As mentioned earlier, this extreme rise in TKE in curved models may potentially harm the red blood cells and further activate the platelets in the blood, resulting in many pathological diseases (Ku [25]).

Additionally, contour plots of the TKE for both the non-spiral and spiral flow in model $A1$ in Fig. 21 also show that the maximum TKE increases for the spiral flow (frame b), though it decreases along the centreline for the spiral flow as reported

by Paul and Larman [4]. Therefore, taking only the centreline data for TKE would provide an incomplete description of the spiralling effects.

Furthermore, it can be observed that the effect of the spiral flow on the maximum blood pressure drop (Fig. 22) and the maximum WSS (Fig. 23) in any model for all the Reynolds numbers is very insignificant. However, the effect of the upstream curved segment on the maximum blood-pressure drop and the maximum WSS is clearly seen. For instance, the maximum blood pressure drop increases $\approx 7\%$ in the 120° curved upstream model from its minimum value in the straight stenosed tube for all the investigated Reynolds numbers. On the other hand, the maximum WSS increases $\approx 3\%$, $\approx 1.5\%$, $\approx 3\%$ and $\approx 4\%$ in the 120° curved upstream model from its minimum value in the straight stenosed tube for $Re = 500$, 1000, 1500 and 2000 respectively. Thus, the stenosis in curved artery increases the risk of potential rupture and thrombosis as discussed in § 5.4.

# 6 Conclusion

The standard $k$-$\omega$ transitional model and LES were applied to study the effects of the spiral blood flow in various stenosed arterial models with an effect of curvature placed upstream at various angles. The results presented in the paper generally show that the spiral blood flow slightly increases the recirculation zone in the straight stenosed tube. Moreover, depending on the flow Reynolds number and model geometry the influence of the spiral blood flow may also moderately increase the turbulence kinetic energy in the post-stenosis region.

As for the effects of the upstream curved segment, the maximum TKE increases significantly in the 120° curved upstream model from its minimum value found in the straight stenosed tube for $Re = 1000$, 1500 and 2000. But, it decreases dramatically compared to that obtained in the 60° curved upstream model for $Re = 500$. Additionally, the maximum pressure drop and the maximum WSS increase in the 120° curved upstream model from their corresponding minimum values in the

straight stenosed tube for all the Reynolds numbers.

Though, in this study, the walls of the models are taken rigid instead of biologically realistic distensible wall, this paper potentially gives some understanding of the effects of the spiral velocity in the post-stenotic region. The study in this paper was also simplified by considering the steady flow in the arterial stenosis models, whereas the blood flow is physiologically pulsatile. A thorough numerical investigation of the physiologically pulsatile spiral blood flow in stenosed (distensible) arteries is a natural extension of this paper. Moreover, a simplified tangential velocity was introduced at the inlet of the arterial models to generate the steady-state spiral flow. Further study is thus also required to better implement the feature of the heart twisting and blood flow spiralling through arteries.

## Acknowledgment

Funding from the School of Engineering of the University of Glasgow and from the SORSAS are acknowledged gratefully by the first author.

## References

[1] P. A. Stonebridge, C. M. Brophy, Spiral laminar flow in arteries?, The Lancet 338 (1991) 1360–1361.

[2] P. A. Stonebridge, P. R. Hoskins, P. L. Allan, J. F. F. Belch, Spiral laminar flow in vivo, Clinical Science 91 (1996) 17–21.

[3] P. A. Stonebridge, C. Buckley, A. Thompson, J. Dick, G. Hunter, J. A. Chudek, J. G. Houston, J. J. F. Belch, Non spiral and spiral (helical) flow patterns in stenoses—in vitro observations using spin and gradient echo magnetic resonance imaging (mri) and computational fluid dynamic modeling, International Angiology 23 (3) (2004) 276–283.

[4] M. C. Paul, A. Larman, Investigation of spiral blood flow in a model of arterial stenosis, Medical Engineering & Physics 31 (2009) 1195–1203.

[5] M. D. Deshpande, D. P. Giddens, Turbulence measurements in a constricted tube, J. Fluid Mech. 97 (1979) 65–89.

[6] F. Ghalichi, X. Deng, A. De Champlain, Y. Douville, M. King, R. Guidoin, Low Reynolds number turbulence modeling of blood flow in arterial stenoses, Biorheology 35 (4-5) (1998) 281–294.

[7] S. S. Varghese, S. H. Frankel, Numerical Modeling of pulsatile turbulent flow in stenotic vessels, ASME J. Biomech. Eng. 125 (2003) 445–460.

[8] T. S. Lee, W. Liao, H. T. Low, Numerical simulation of turbulent flow through series stenoses, Int. J. Numer. Meth. Fluids 42 (2003) 717–740.

[9] T. S. Lee, W. Liao, H. T. Low, Numerical study of physiological turbulent flows through series arterial stenoses, Int. J. Numer. Meth. Fluids 46 (2004) 315–344.

[10] M. X. Li, J. J. Beech-Brandt, L. R. John, P. R. Hoskins, W. J. Easson, Numerical Analysis of pulsatile blood flow and vessel wall mechanics in different degrees of stenoses, J. Biomechanics 40 (2007) 3715–3724.

[11] S. S. Varghese, S. H. Frankel, P. F. Fischer, Modelling transition to turbulence in eccentric stenotic flows, ASME J. Biomech. Eng. 130 (2008) 0145031–7.

[12] M. C. Paul, M. M. Molla, G. Roditi, Large-eddy simulation of pulsatile blood flow, Medical Engineering & Physics 31 (2009) 153159.

[13] M. M. Molla, M. C. Paul, G. Roditi, Les of additive and non-additive pulsatile flows in a model arterial stenosis, Computer Methods in Biomechanics and Biomedical Engineering 13 (1) (2010) 105–120.

[14] M. M. Molla, M. C. Paul, Les of non-newtonian physiological blood flow in a model of arterial stenosis, Medical Engineering & Physics 34 (2012) 1079–1087.

[15] M. C. Paul, M. M. Molla, Investigation of physiological pulsatile flow in a model of arterial stenosis using large-eddy and direct numerical simulations, Applied Mathematical Modelling 36 (2012) 4393–4413.

[16] F. P. P. Tan, N. B. Wood, G. Tabor, X. Y. Xu, Comparison of les of steady transitional flow in an idealized stenosed axisymmetric artery model with a rans transitional model, ASME J. Biomech. Eng. 133 (2011) 0510011–12.

[17] R. Gårdhagen, J. Lantz, F. Carlsson, M. Karlsson, Large eddy simmulation of stenotic flow for wall shear stress estimation - validation and application, WSEAS Transactions on Biology and Biomedicine 8 (3) (2011) 86–99.

[18] T. J. Barber, A. Simmons, Large eddy simulation of a stenosed artery using a femoral artery pulsatile flow profile, Artificial Organs 35 (7) (2011) E155–E160.

[19] M. Germano, U. Piomelli, W. Cabot, A dynamic subgrid-scale eddy viscosity model, Physics of Fluids A 3 (7) (1991) 1760–1765.

[20] D. K. Lilly, A Proposed Modification of the Germano Subgrid-Scale Closure Method, Physics of Fluids A 4 (3) (1992) 633–635.

[21] S. E. Kim, Large eddy simmulation using unstructured meshes and dynamic subgrid-scale turbulence models, Tech. rep., AIAA paper 2004-2548, (34th Fluid Dynamics Conference and Exhibit) (Jun. 2004).

[22] S. A. Ahmed, D. P. Giddens, Flow disturbance measurements through a constricted tube at moderate Reynolds numbers, J. Biomechanics 16 (12) (1983) 955–963.

[23] S. A. Ahmed, D. P. Giddens, Velocity measurement in steady flow through axisymmetric stenosis at moderate Reynolds number, J. Biomechanics 16 (7) (1983) 505–516.

[24] D. F. Young, Fluid mechanics of arterial stenoses, ASME J. Biomech. Eng. 101 (1979) 157–173.

[25] D. N. Ku, Blood flows in arteries, Annu. Rev. Fluid Mechanics 29 (1997) 399–434.

[26] T. J. Pedley, The fluid mechanics of large blood vessels, Cambridge University Press, 1980.

[27] Y. C. Fung, Biomechanics: Circulation, 2nd Edition, Springer, 1997.

[28] Fluent Inc., Fluent 6.3: User's Guide (Sep. 2006).

[29] J. Ryval, A. G. Straatman, D. A. Steinman, Two-equation turbulence modelling of pulsatile flow in a stenosed tube, ASME J. Biomech. Eng. 126 (2004) 625–635.

[30] J. P. Vandoormaal, G. D. Raithby, Enhancements of the simple method for predicting incompressible fluid flows, Numer. Heat Transfer 7 (1984) 147–163.

[31] R. I. Issa, Solution of implicitly discretized fluid flow equations by operator splitting, J. Computational Physics 62 (1986) 40–65.

[32] C. M. Rhie, W. L. Chow, Numerical study of the turbulent flow past an airfoil with trailing edge separation, AIAA Journal 21 (11) (1983) 1525–1532.

[33] A. Frydrychowicz, A. Harloff, B. Jung, M. Zaitsev, E. W. Eigang, T. A. Bley, M. Langer, J. Henning, M. Markl, Time-resolved, 3-Dimensional magnetic resonance flow analysis at 3 T: visualization of normal and pathological aortic vascular hemodynamics, J. Comput. Assist. Tomogr. 31(1) (2007) 9–15.

[34] D. M. Wootton, D. N. Ku, Fluid mechanics of vascular systems, diseases, and thrombosis, Annu. Rev. Biomed. Eng. 01 (1999) 299–329.

[35] Z.-Y. Li, V. Taviani, T. Tang, U. Sadat, V. Young, A. Patterson, M. Graves, J. H. Gillard, The mechanical triggers of plaque rupture: shear stress vs pressure gradient, The British Journal of Radiology 82 (2009) S39–S45.

[36] A. M. Malek, S. L. Alper, S. Izumo, Hemodynamic shear stress and its role in atherosclerosis, J. Ameriacn Medical Association (JAMA) 282 (1999) 2035–2042.

[37] D. L. Fry, Acute vascular endothelial changes associated with increased blood velocity gradients, Circulation Res. 22 (1968) 165–197.

[38] J. D. Folts, E. B. Crowell Jr., G. G. Rowe, Platelet aggregation in partially obstructed vessels and its elimination with aspirin, Circulation 54 (3) (1976) 365–370.

[39] S. P. Sutera, M. H. Mehrjardi, Deformation and fragmentation of human red blood cells in turbulent flow, Biophysical J. 15 (1975) 1–10.

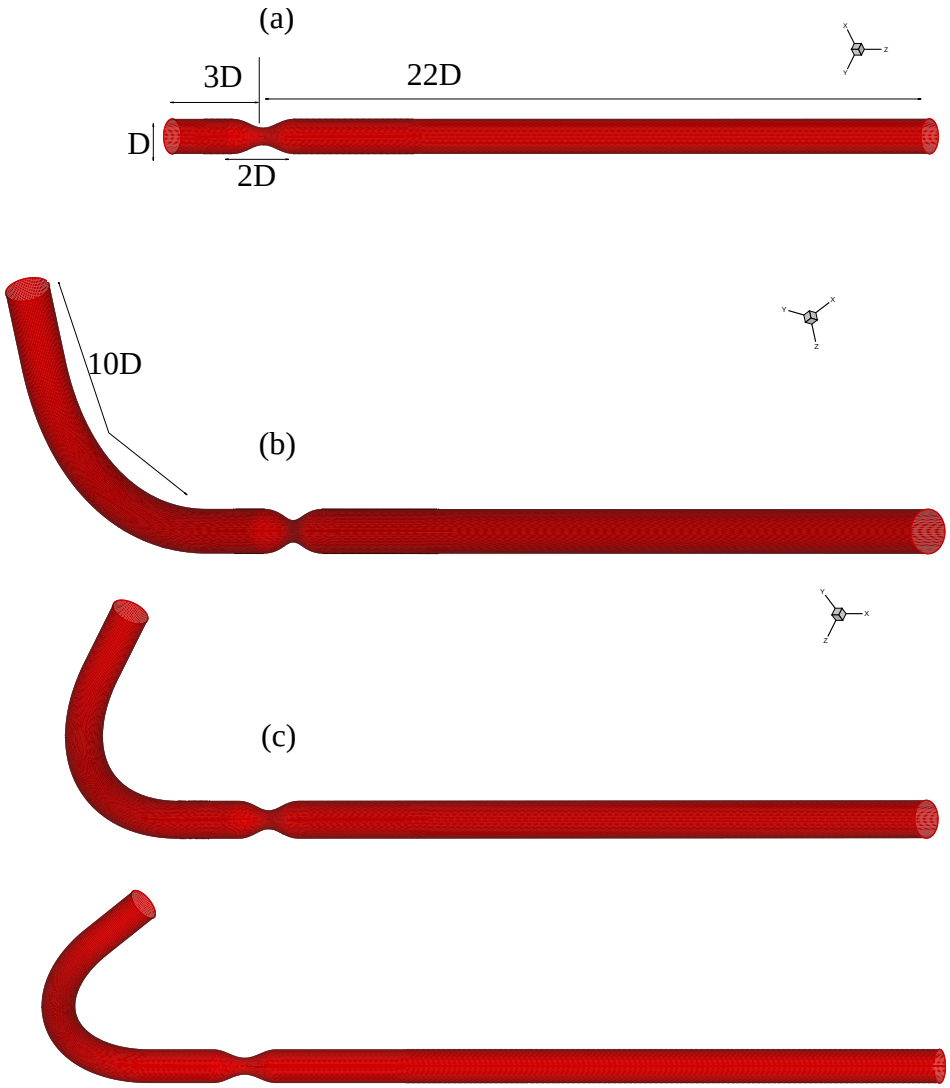


Figure 1: Three dimensional view of the model arteries without and with an upstream curved section of varying angles of curvature ($\theta$). Angle of curvature ($\theta$) in frame (a), (b), (c) and (d), is 0°, 60°, 90° and 120° respectively.

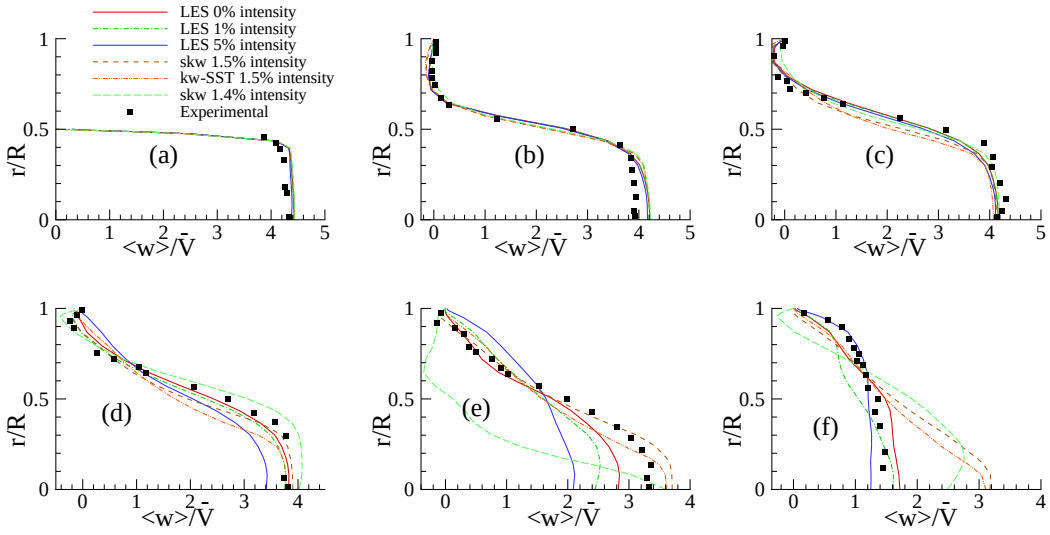


Figure 2: Axial velocity comparison with the experimental data of Ahmed and Giddens [22] for the non-spiral flow in model $B1$ at (a) $z/D = 0$, (b) $z/D = 1$, (c) $z/D = 2.5$, (d)$z/D = 4$, (e) $z/D = 5$ and (f) $z/D = 6$.

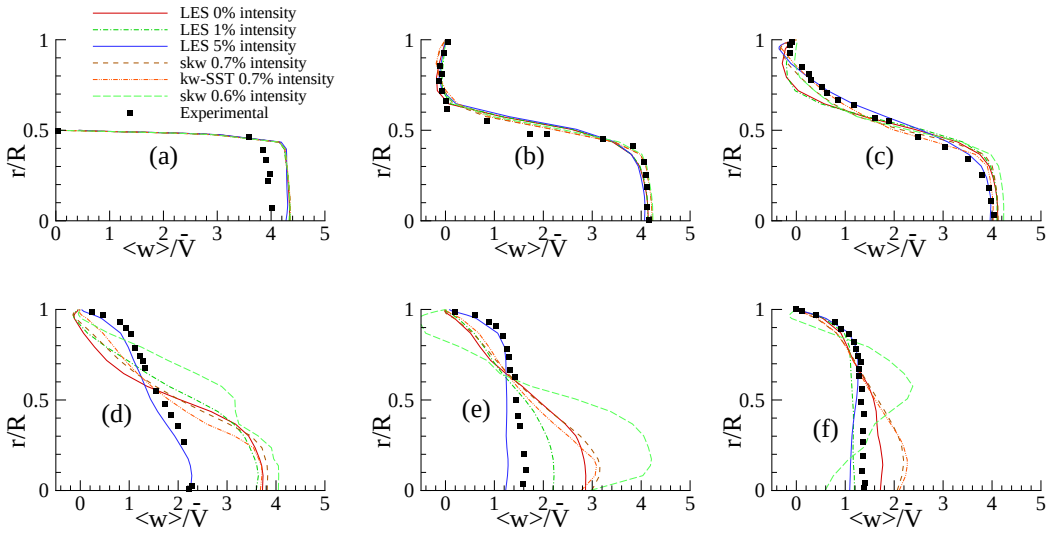


Figure 3: Axial velocity comparison with the experimental data of Ahmed and Giddens [23] for the non-spiral flow in model $D1$ at (a) $z/D = 0$, (b) $z/D = 1$, (c) $z/D = 2.5$, (d)$z/D = 4$, (e) $z/D = 5$ and (f) $z/D = 6$.

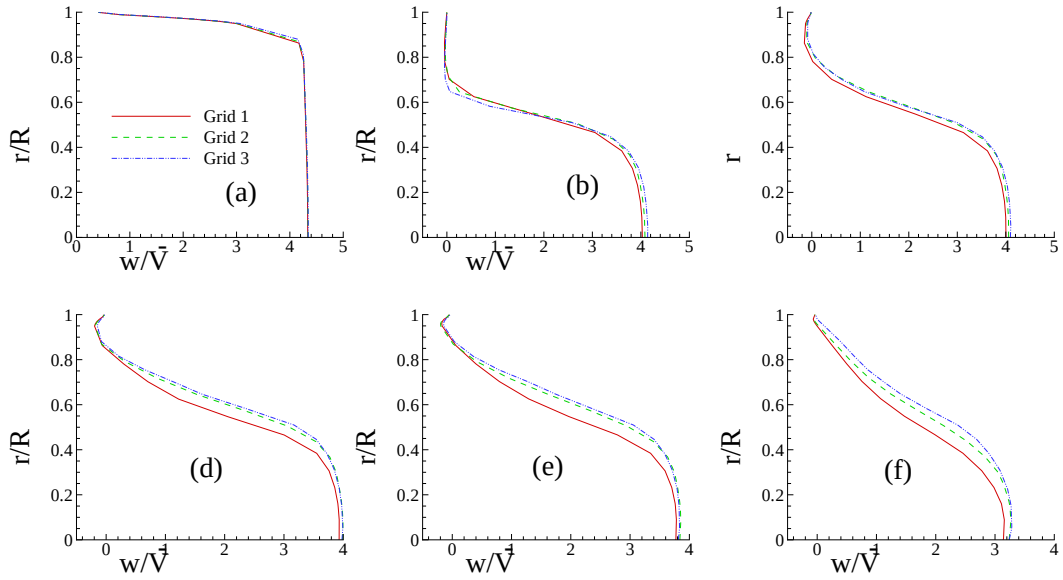


Figure 4: Grid resolution study for LES of the spiral flow in model $D1$ showing the axial velocity at (a) $z/D = 0$, (b) $z/D = 1$, (c) $z/D = 2.5$, (d) $z/D = 4$, (e) $z/D = 5$ and (f) $z/D = 6$.

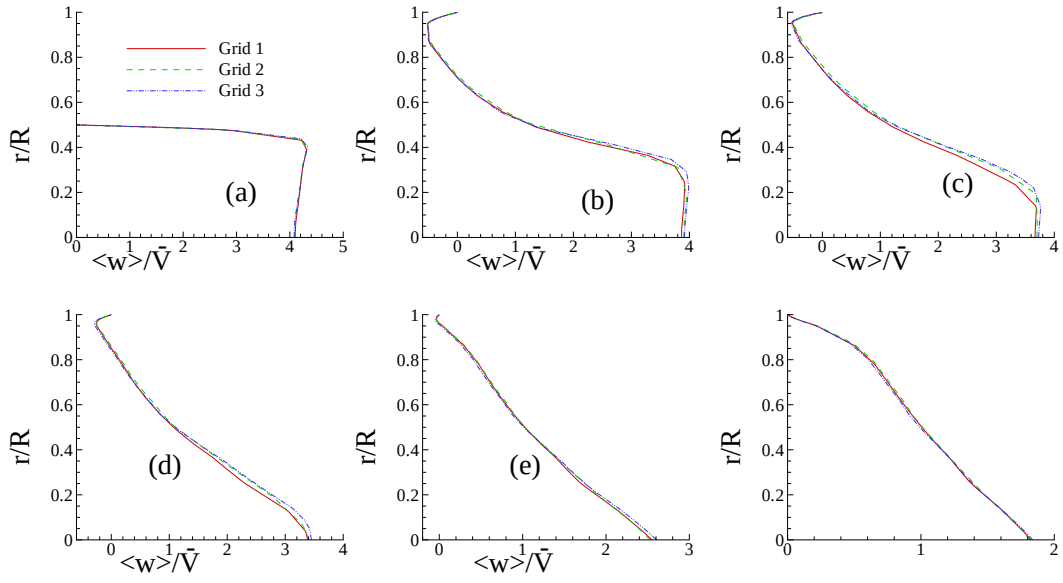


Figure 5: Grid resolution study for the spiral flow in model $D3$ with the $k - \omega$ Transitional approach showing the axial velocity at (a) $z/D = 0$, (b) $z/D = 1$, (c) $z/D = 2.5$, (d)$z/D = 4$, (e) $z/D = 5$ and (f) $z/D = 6$.

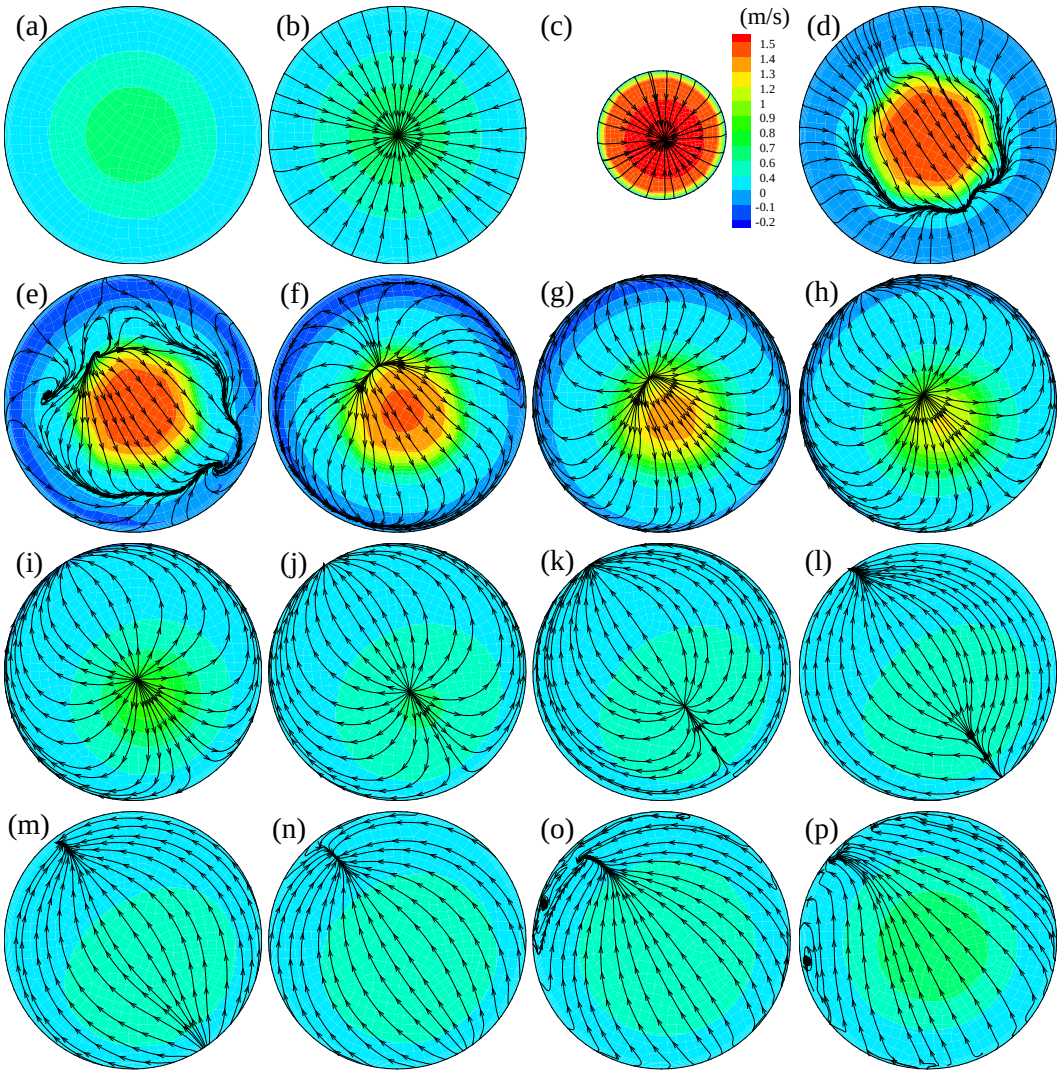


Figure 6: Cross-sectional streamlines appended on the axial velocity contour for the non-spiral flow in model $D1$ at (a) $z/D = -3$, (b) $z/D = -1$, (c) $z/D = 0$, (d) $z/D = 1$, (e) $z/D = 2$, (f) $z/D = 3$, (g) $z/D = 4$, (h) $z/D = 5$, (i) $z/D = 6$, (j) $z/D = 7$, (k) $z/D = 8$, (l) $z/D = 9$, (m) $z/D = 10$, (n) $z/D = 12$, (o) $z/D = 16$ and (p) $z/D = 22$.

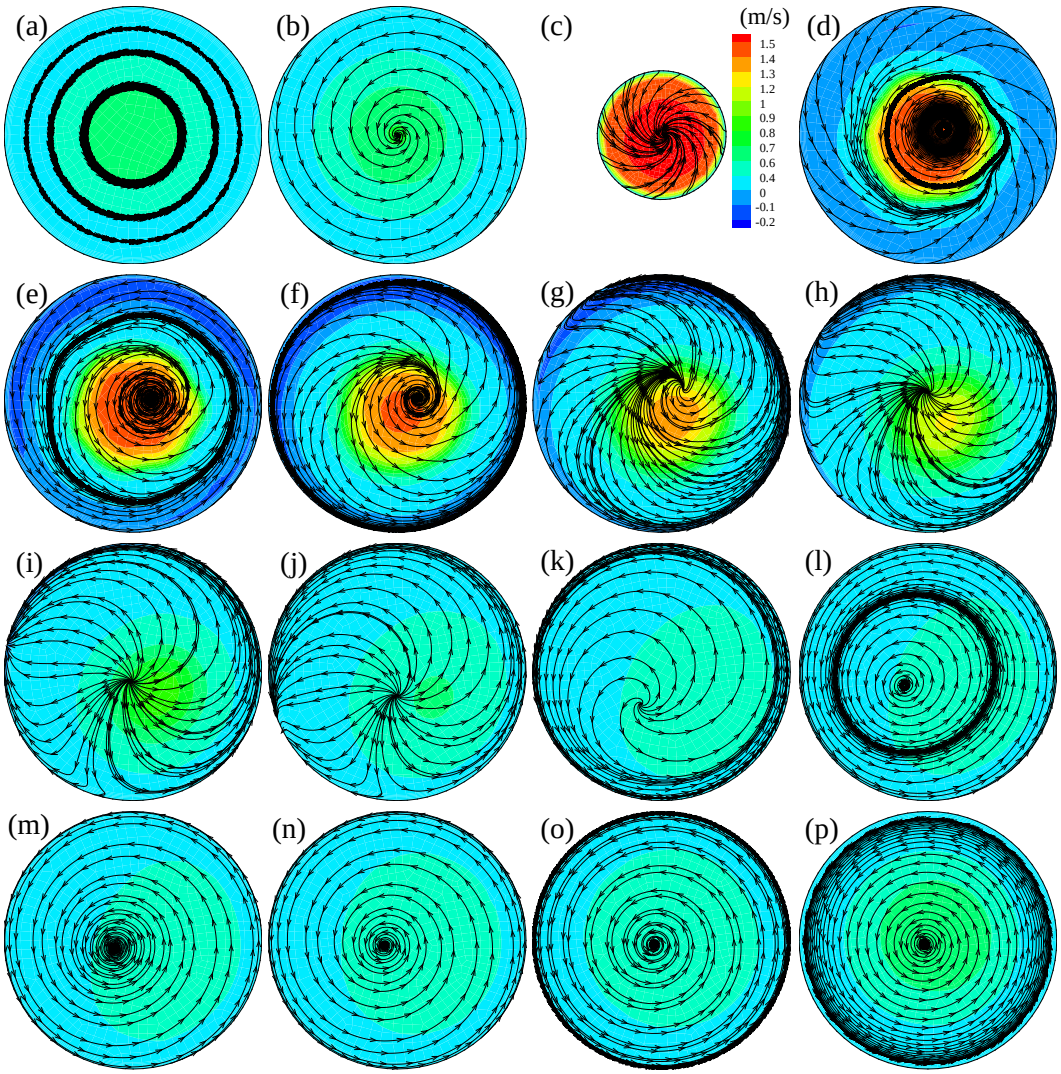


Figure 7: Cross-sectional streamlines appended on the axial velocity contour for the spiral flow in model $D1$ at (a) $z/D = -3$, (b) $z/D = -1$, (c) $z/D = 0$, (d) $z/D = 1$, (e) $z/D = 2$, (f) $z/D = 3$, (g) $z/D = 4$, (h) $z/D = 5$, (i) $z/D = 6$, (j) $z/D = 7$, (k) $z/D = 8$, (l) $z/D = 9$, (m) $z/D = 10$, (n) $z/D = 12$, (o) $z/D = 16$ and (p) $z/D = 22$.

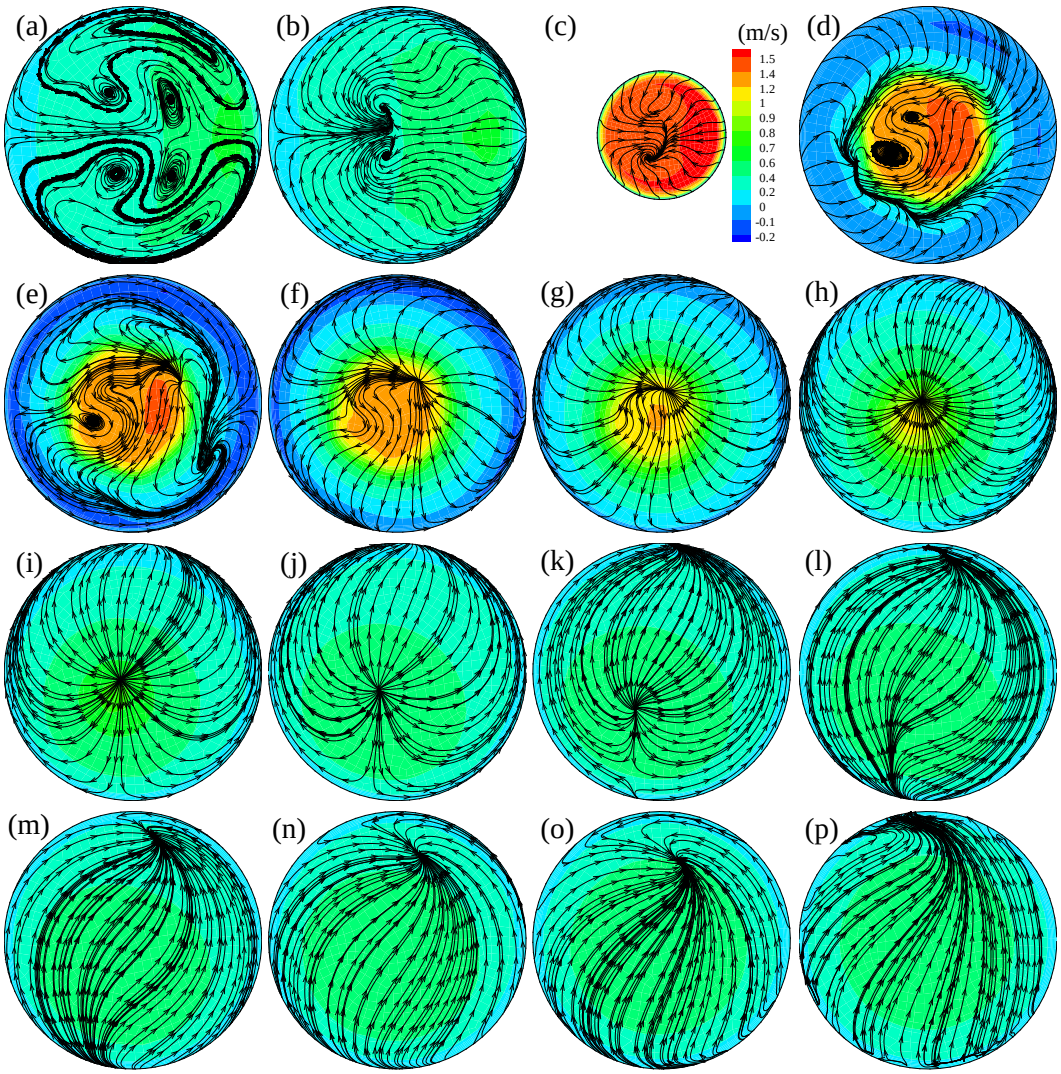


Figure 8: Cross-sectional streamlines appended on the axial velocity contour for the non-spiral flow in model $D3$ at (a) $z/D = -3$, (b) $z/D = -1$, (c) $z/D = 0$, (d) $z/D = 1$, (e) $z/D = 2$, (f) $z/D = 3$, (g) $z/D = 4$, (h) $z/D = 5$, (i) $z/D = 6$, (j) $z/D = 7$, (k) $z/D = 8$, (l) $z/D = 9$, (m) $z/D = 10$, (n) $z/D = 12$, (o) $z/D = 16$ and (p) $z/D = 22$.

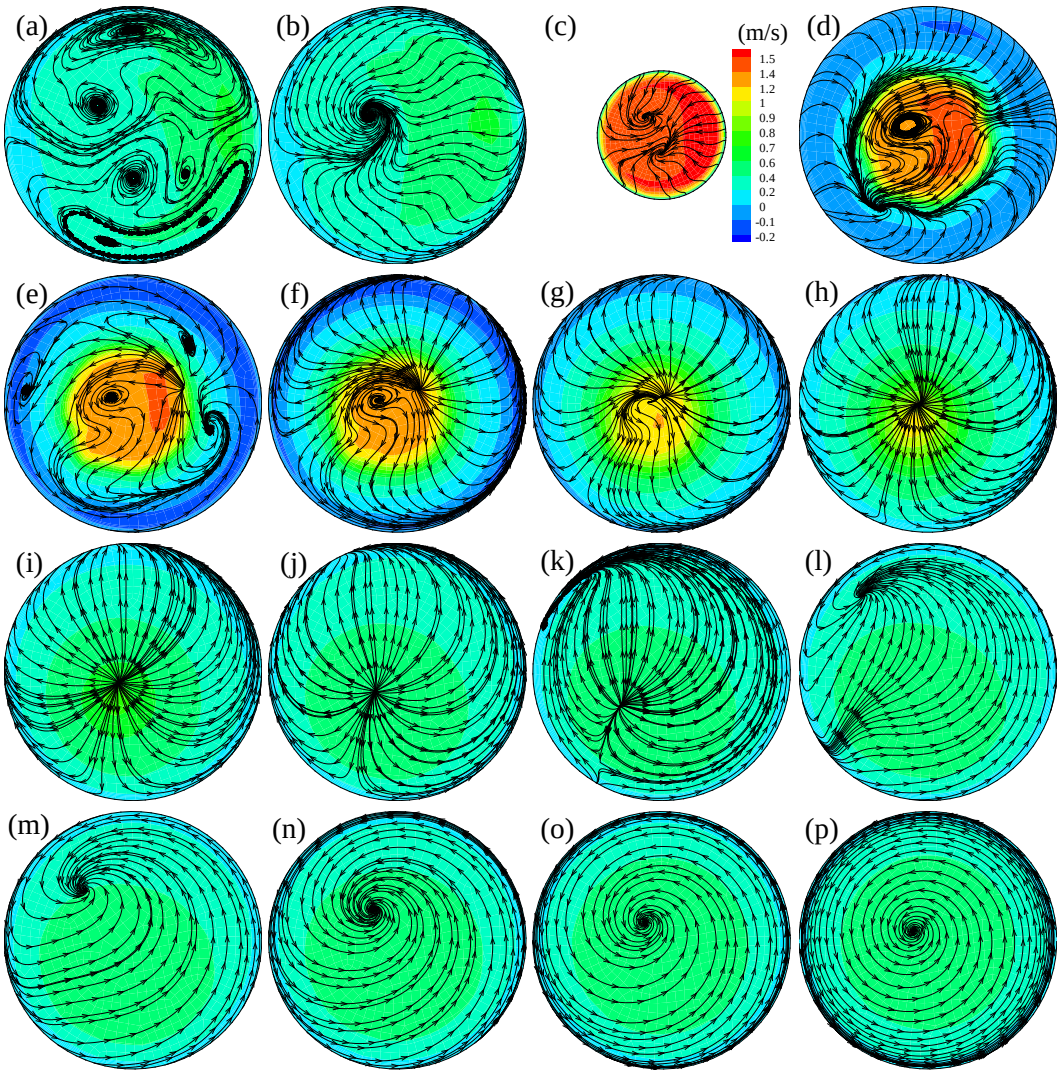


Figure 9: Cross-sectional streamlines appended on the axial velocity contour for the spiral flow in model $D3$ at (a) $z/D = -3$, (b) $z/D = -1$, (c) $z/D = 0$, (d) $z/D = 1$, (e) $z/D = 2$, (f) $z/D = 3$, (g) $z/D = 4$, (h) $z/D = 5$, (i) $z/D = 6$, (j) $z/D = 7$, (k) $z/D = 8$, (l) $z/D = 9$, (m) $z/D = 10$, (n) $z/D = 12$, (o) $z/D = 16$ and (p) $z/D = 22$.

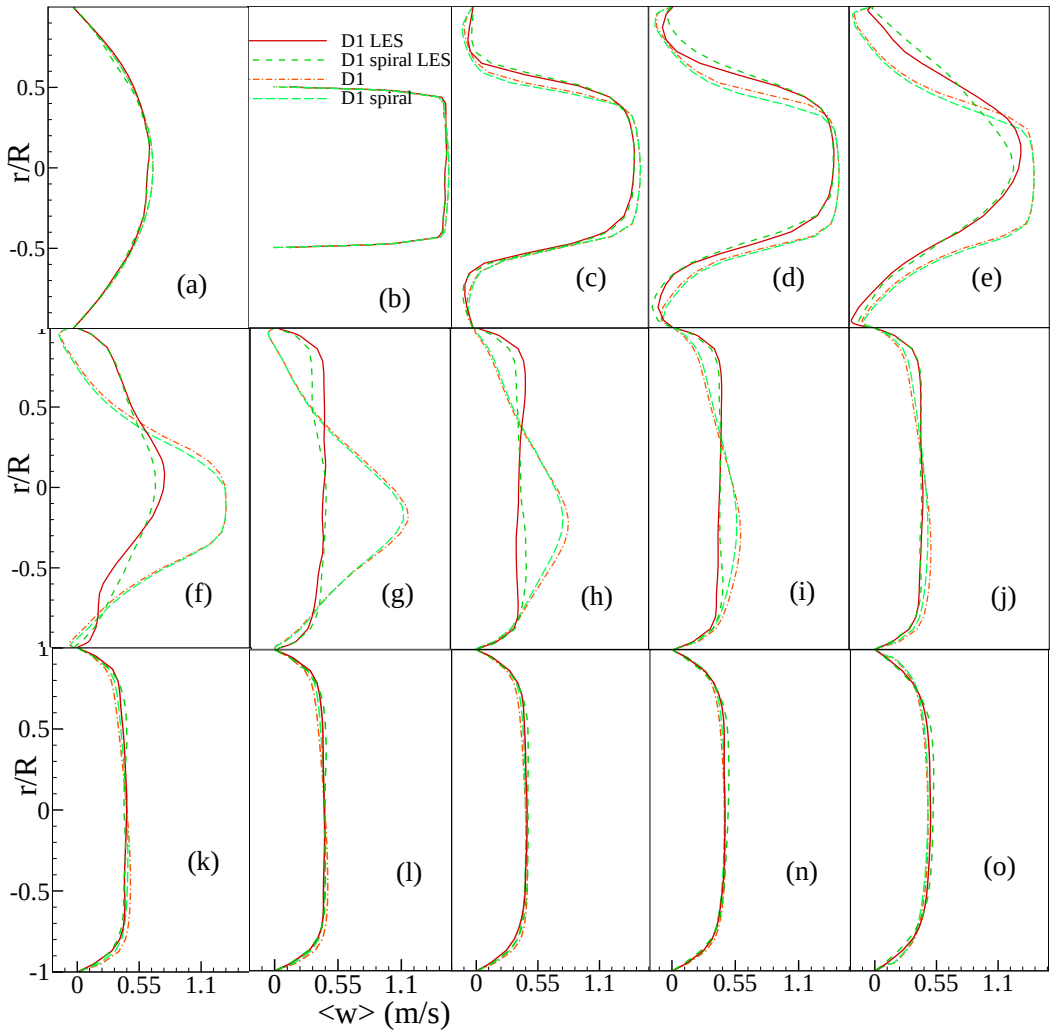


Figure 10: Mean axial velocity, $\langle w \rangle$, profiles for both the non-spiral and spiral flow in model $D1$ at (a) $z/D = -1$, (b) $z/D = 0$, (c) $z/D = 1$, (d) $z/D = 2$, (e) $z/D = 3$, (f) $z/D = 4$, (g) $z/D = 5$, (h) $z/D = 6$, (i) $z/D = 7$, (j) $z/D = 8$, (k) $z/D = 9$, (l) $z/D = 10$, (m) $z/D = 12$, (n) $z/D = 16$ and (o) $z/D = 22$. Note that LES was also applied to this model.

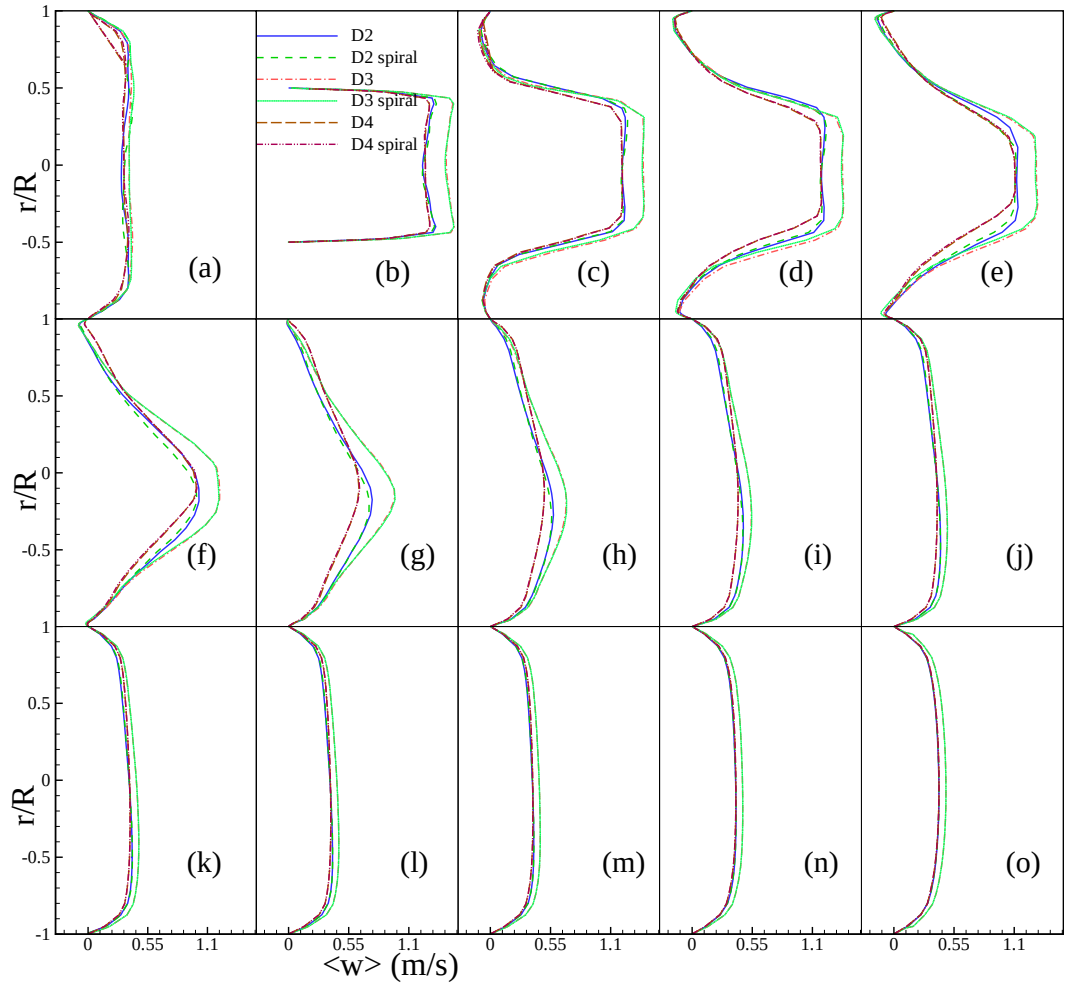


Figure 11: Mean axial velocity, $\langle w \rangle$, profiles for both the non-spiral and spiral flow in models $D2$, $D3$ and $D4$ at (a) $z/D = -1$, (b) $z/D = 0$, (c) $z/D = 1$, (d) $z/D = 2$, (e) $z/D = 3$, (f) $z/D = 4$, (g) $z/D = 5$, (h) $z/D = 6$, (i) $z/D = 7$, (j) $z/D = 8$, (k) $z/D = 9$, (l) $z/D = 10$, (m) $z/D = 12$, (n) $z/D = 16$ and (o) $z/D = 22$.

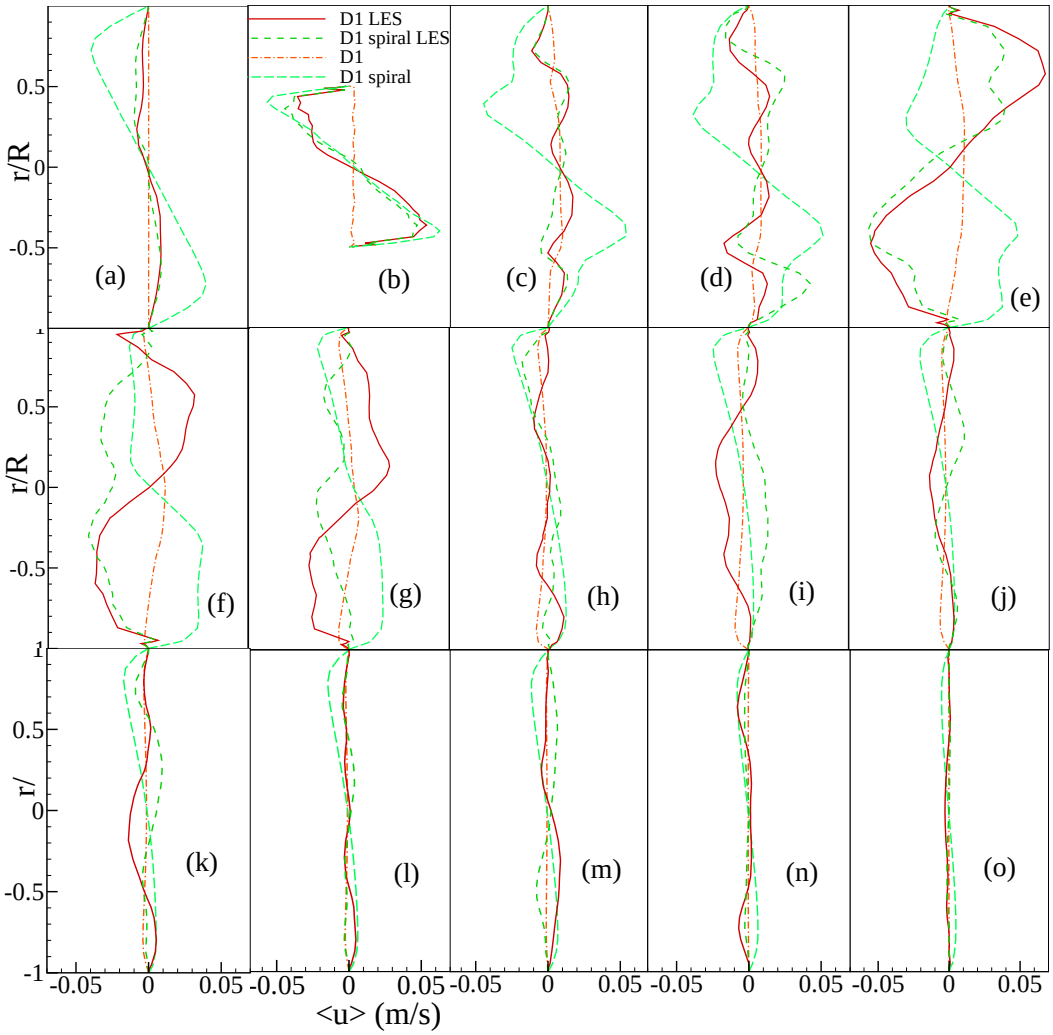


Figure 12: Mean $x$-velocity (radial), $\langle u \rangle$, profiles for both the non-spiral and spiral flow in model $D1$ at (a) $z/D = -1$, (b) $z/D = 0$, (c) $z/D = 1$, (d) $z/D = 2$, (e) $z/D = 3$, (f) $z/D = 4$, (g) $z/D = 5$, (h) $z/D = 6$, (i) $z/D = 7$, (j) $z/D = 8$, (k) $z/D = 9$, (l) $z/D = 10$, (m) $z/D = 12$, (n) $z/D = 16$ and (o) $z/D = 22$. Note that LES was also applied to this model.

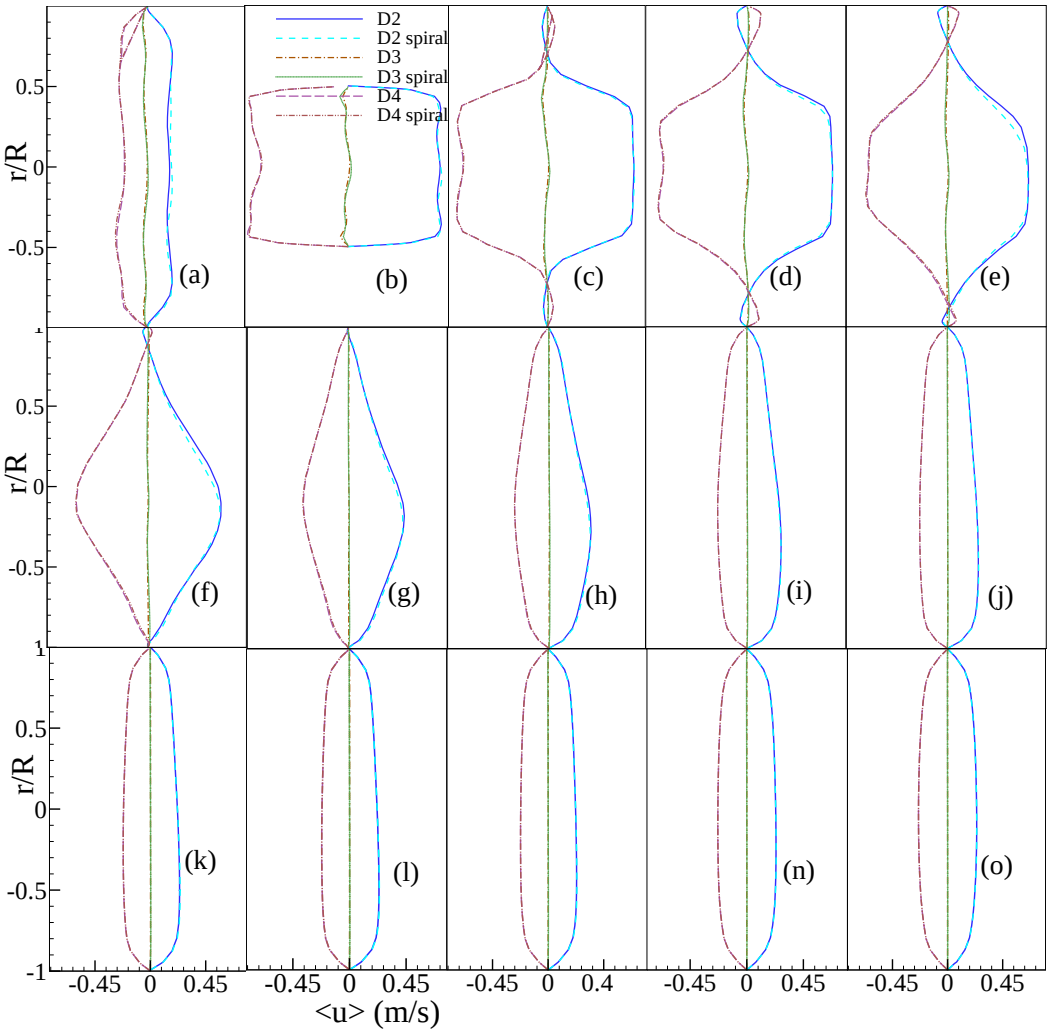


Figure 13: Mean $x$-velocity (radial), $\langle u \rangle$, profiles for both the non-spiral and spiral flow in models $D2$, $D3$ and $D4$ at (a) $z/D = -1$, (b) $z/D = 0$, (c) $z/D = 1$, (d) $z/D = 2$, (e) $z/D = 3$, (f) $z/D = 4$, (g) $z/D = 5$, (h) $z/D = 6$, (i) $z/D = 7$, (j) $z/D = 8$, (k) $z/D = 9$, (l) $z/D = 10$, (m) $z/D = 12$, (n) $z/D = 16$ and (o) $z/D = 22$.

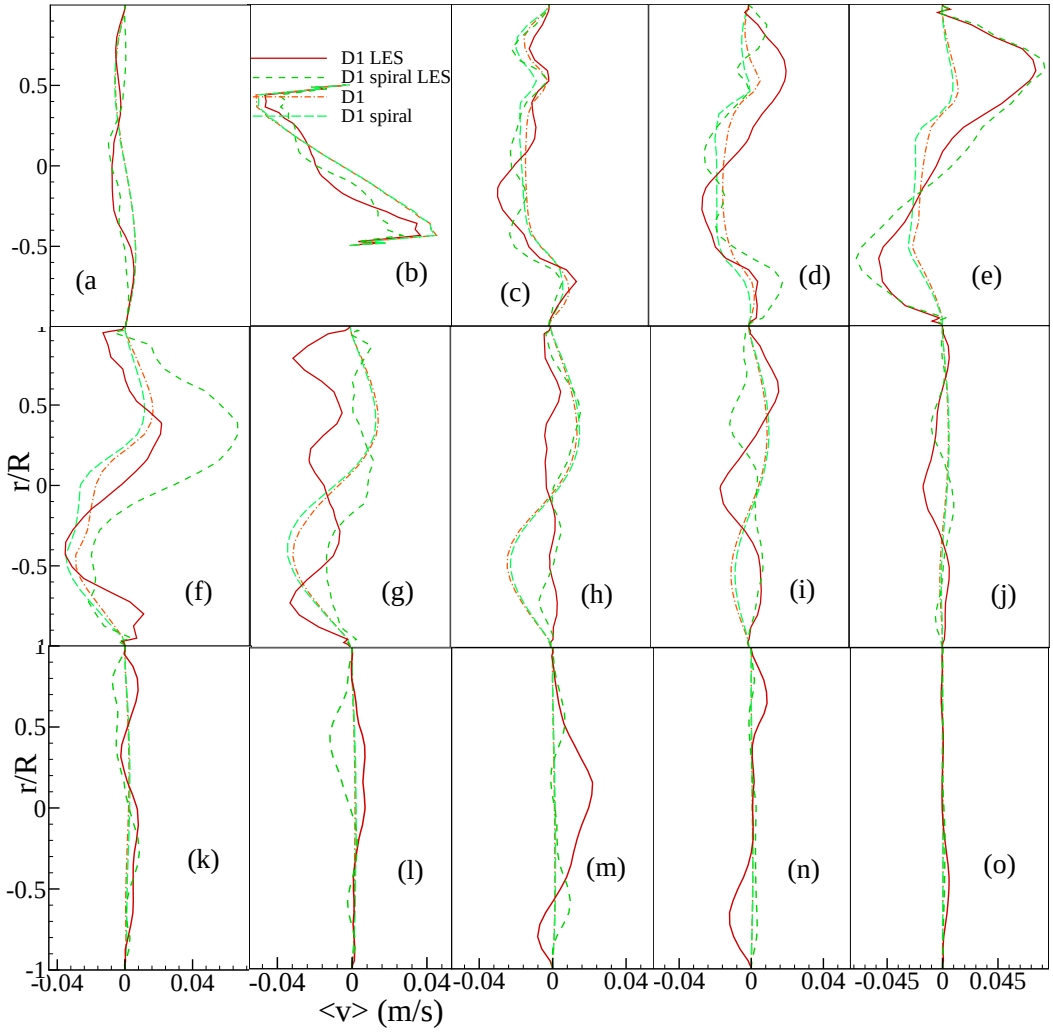


Figure 14: Mean $y$-velocity (tangential), $\langle v \rangle$, profiles for both the non-spiral and spiral flow in model $D1$ at (a) $z/D = -1$, (b) $z/D = 0$, (c) $z/D = 1$, (d) $z/D = 2$, (e) $z/D = 3$, (f) $z/D = 4$, (g) $z/D = 5$, (h) $z/D = 6$, (i) $z/D = 7$, (j) $z/D = 8$, (k) $z/D = 9$, (l) $z/D = 10$, (m) $z/D = 12$, (n) $z/D = 16$ and (o)$z/D = 22$. Note that LES was also applied to this model.

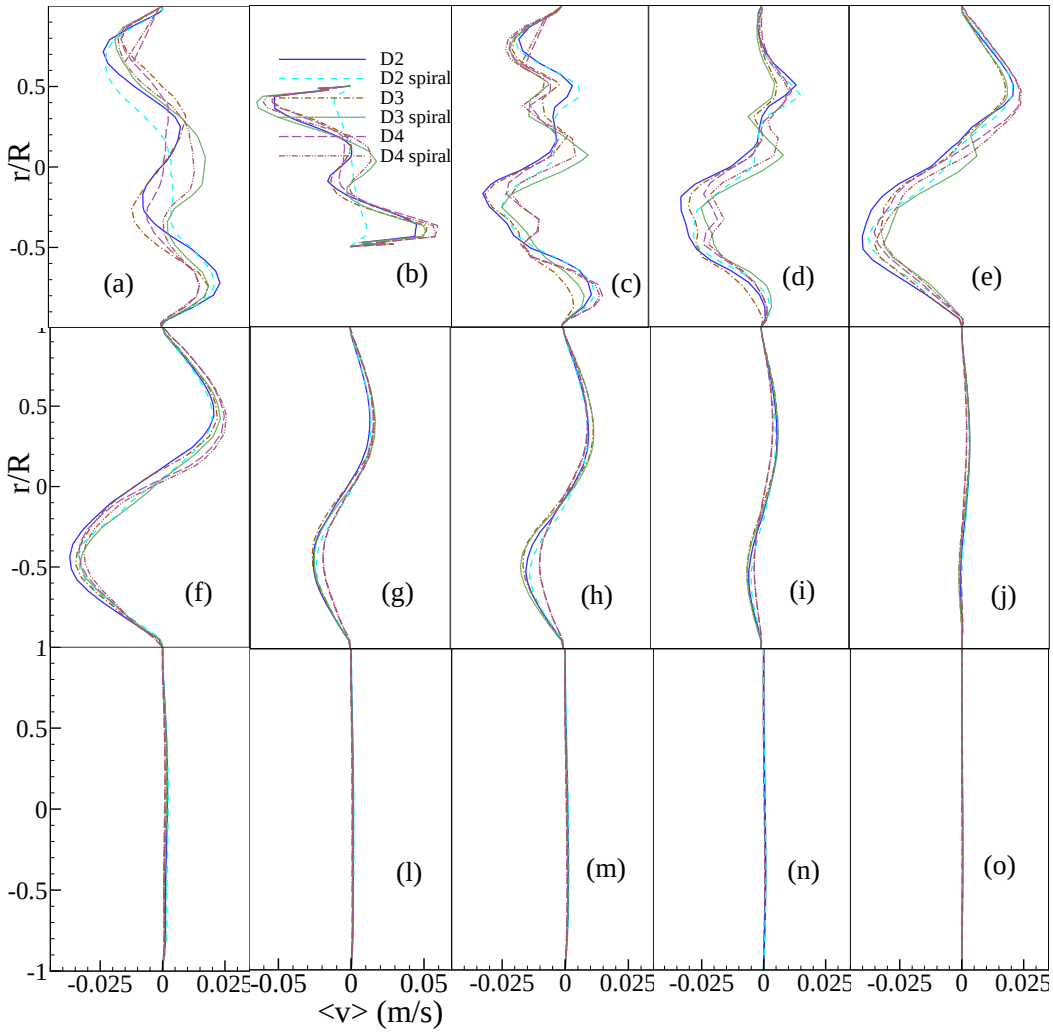


Figure 15: Mean $y$-velocity (tangential), $\langle v \rangle$, profiles for both the non-spiral and spiral flow in models $D2$, $D3$ and $D4$ at (a) $z/D = -1$, (b) $z/D = 0$, (c) $z/D = 1$, (d) $z/D = 2$, (e) $z/D = 3$, (f) $z/D = 4$, (g) $z/D = 5$, (h) $z/D = 6$, (i) $z/D = 7$, (j) $z/D = 8$, (k) $z/D = 9$, (l) $z/D = 10$, (m) $z/D = 12$, (n) $z/D = 16$ and (o)$z/D = 22$.

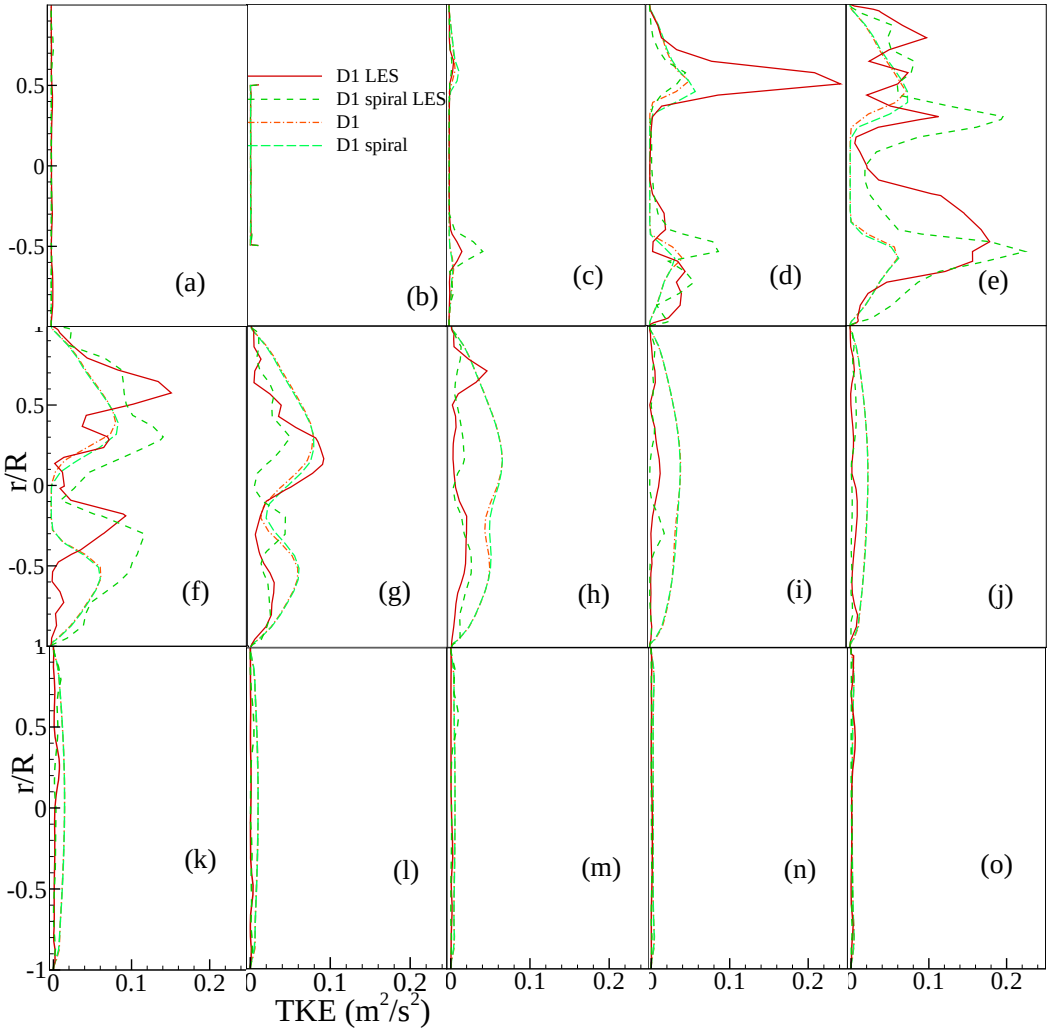


Figure 16: Turbulence kinetic energy, $k$ ($m^2/s^2$), for both the non-spiral and spiral flow in model $D1$ at (a) $z/D = -1$, (b) $z/D = 0$, (c) $z/D = 1$, (d) $z/D = 2$, (e) $z/D = 3$, (f) $z/D = 4$, (g) $z/D = 5$, (h) $z/D = 6$, (i) $z/D = 7$, (j) $z/D = 8$, (k) $z/D = 9$, (l) $z/D = 10$, (m) $z/D = 12$, (n) $z/D = 16$ and (o)$z/D = 22$. Note that LES was also applied to this model.

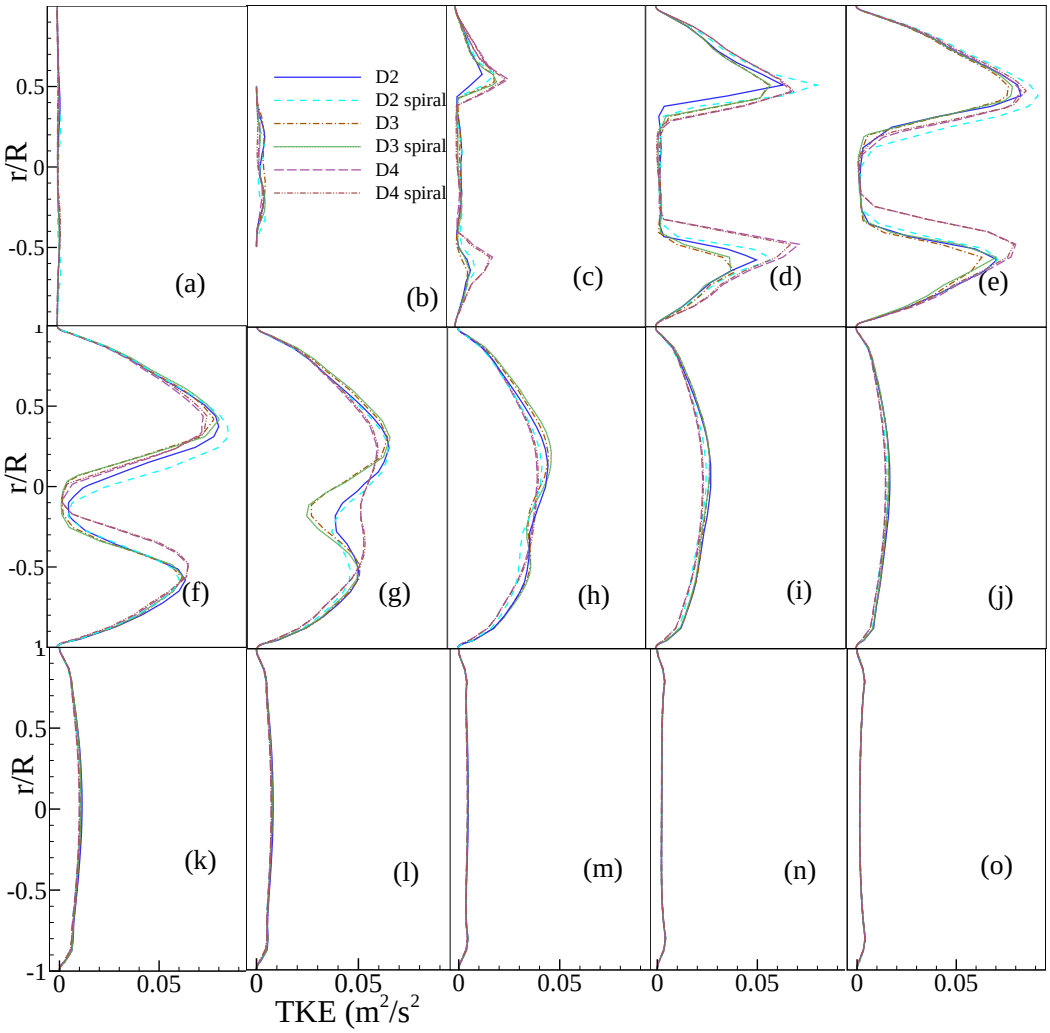


Figure 17: Turbulence kinetic energy, $k$ ($m^2/s^2$), for both the non-spiral and spiral flow in models $D2$, $D3$ and $D4$ at (a) $z/D = -1$, (b) $z/D = 0$, (c) $z/D = 1$, (d) $z/D = 2$, (e) $z/D = 3$, (f) $z/D = 4$, (g) $z/D = 5$, (h) $z/D = 6$, (i) $z/D = 7$, (j) $z/D = 8$, (k) $z/D = 9$, (l) $z/D = 10$, (m) $z/D = 12$, (n) $z/D = 16$ and (o)$z/D = 22$.

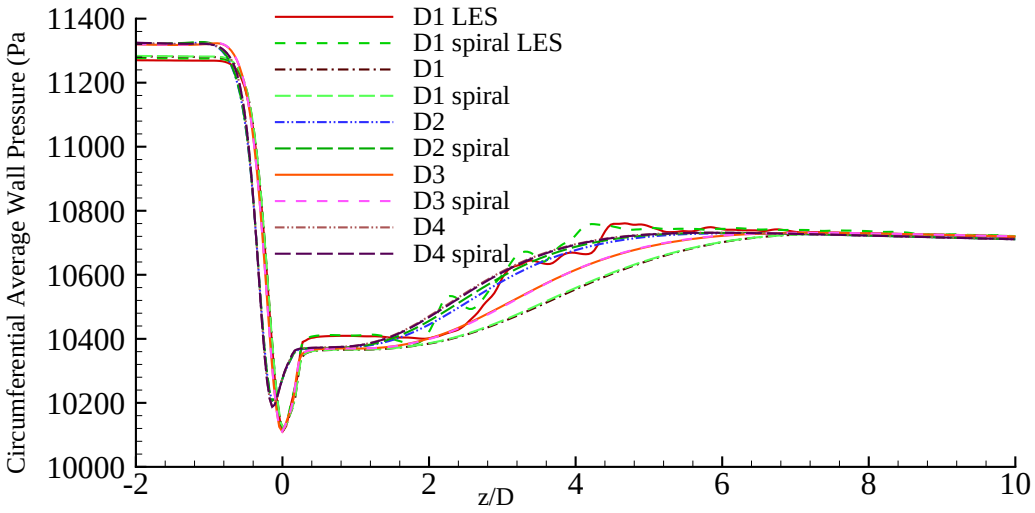


Figure 18: Circumferential average wall pressure (Pa) for both the non-spiral and spiral flow in models $D1$, $D2$, $D3$ and $D4$.

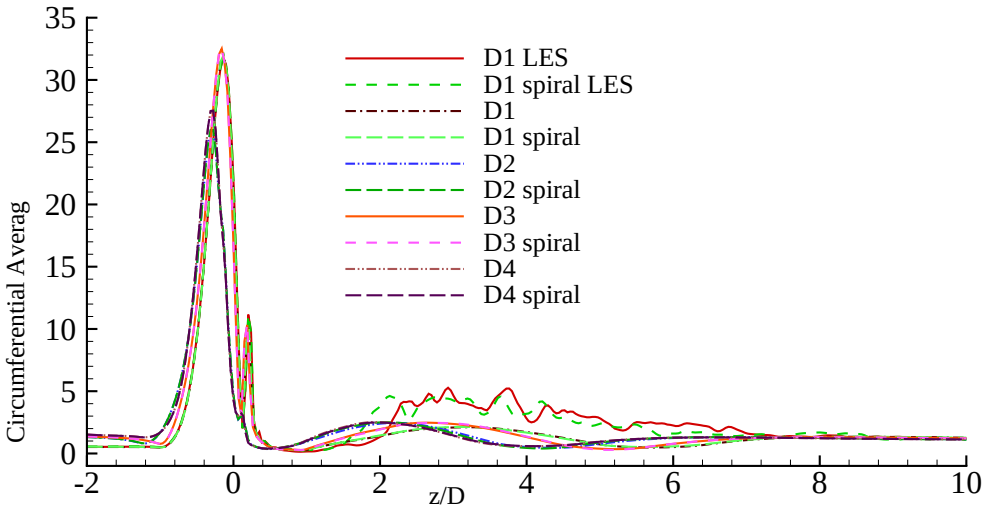


Figure 19: Circumferential average wall shear stress, $\tau$ (Pa), for both the non-spiral and spiral flow in models $D1$, $D2$, $D3$ and $D4$.

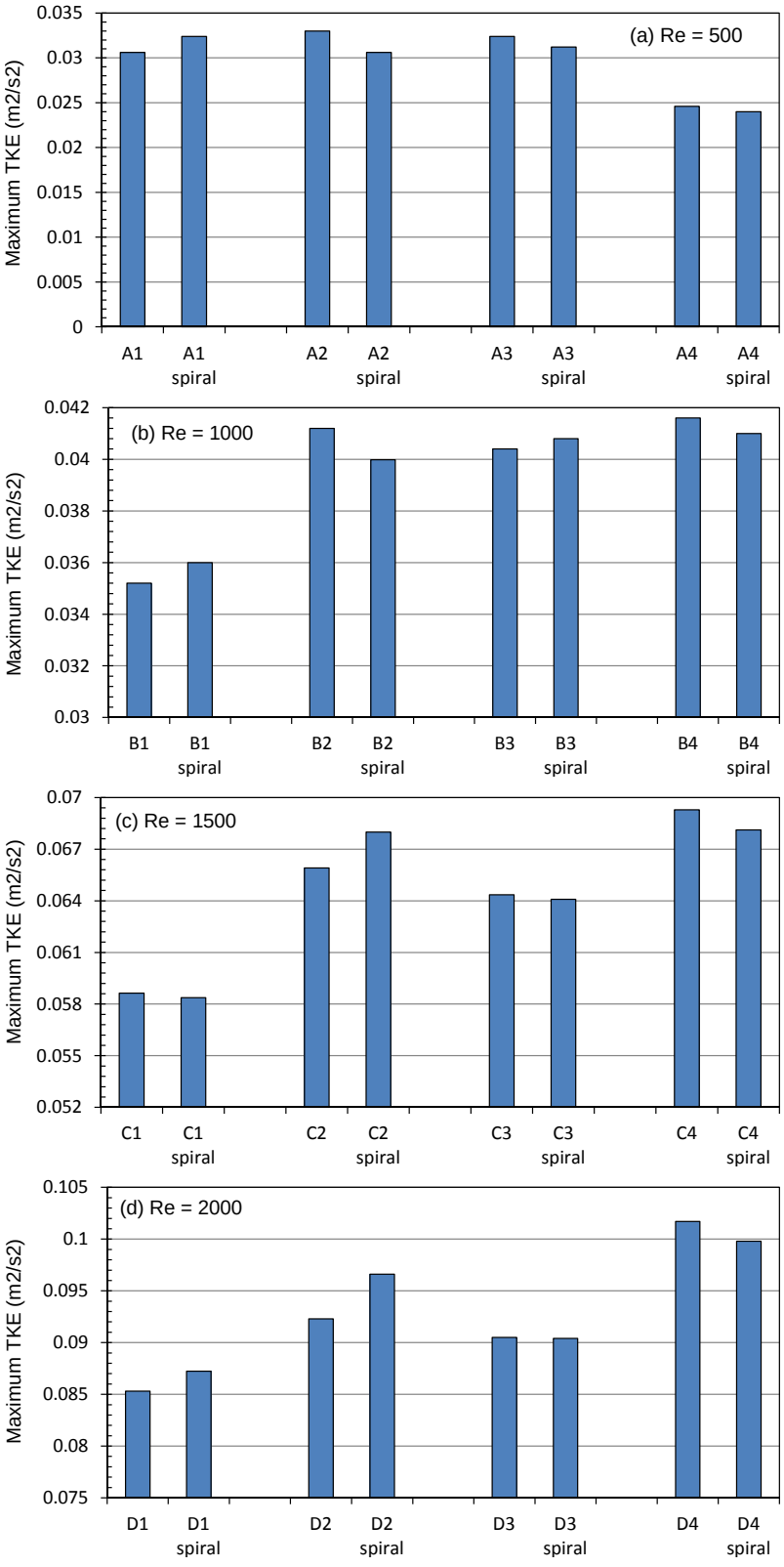


Figure 20: Bar charts of the maximum turbulence kinetic energy for both the non-spiral and spiral flow in all models for (a) $Re = 500$, (b) $Re = 1000$, (c) $Re = 1500$ and (d) 2000.

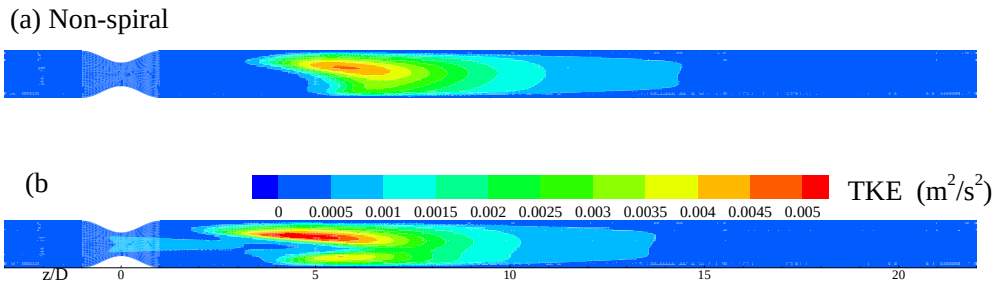


Figure 21: Contour plots of the TKE, k ($m^2/s^2$), in model $A1$ for (a) the non-spiral flow and (b) the spiral flow.

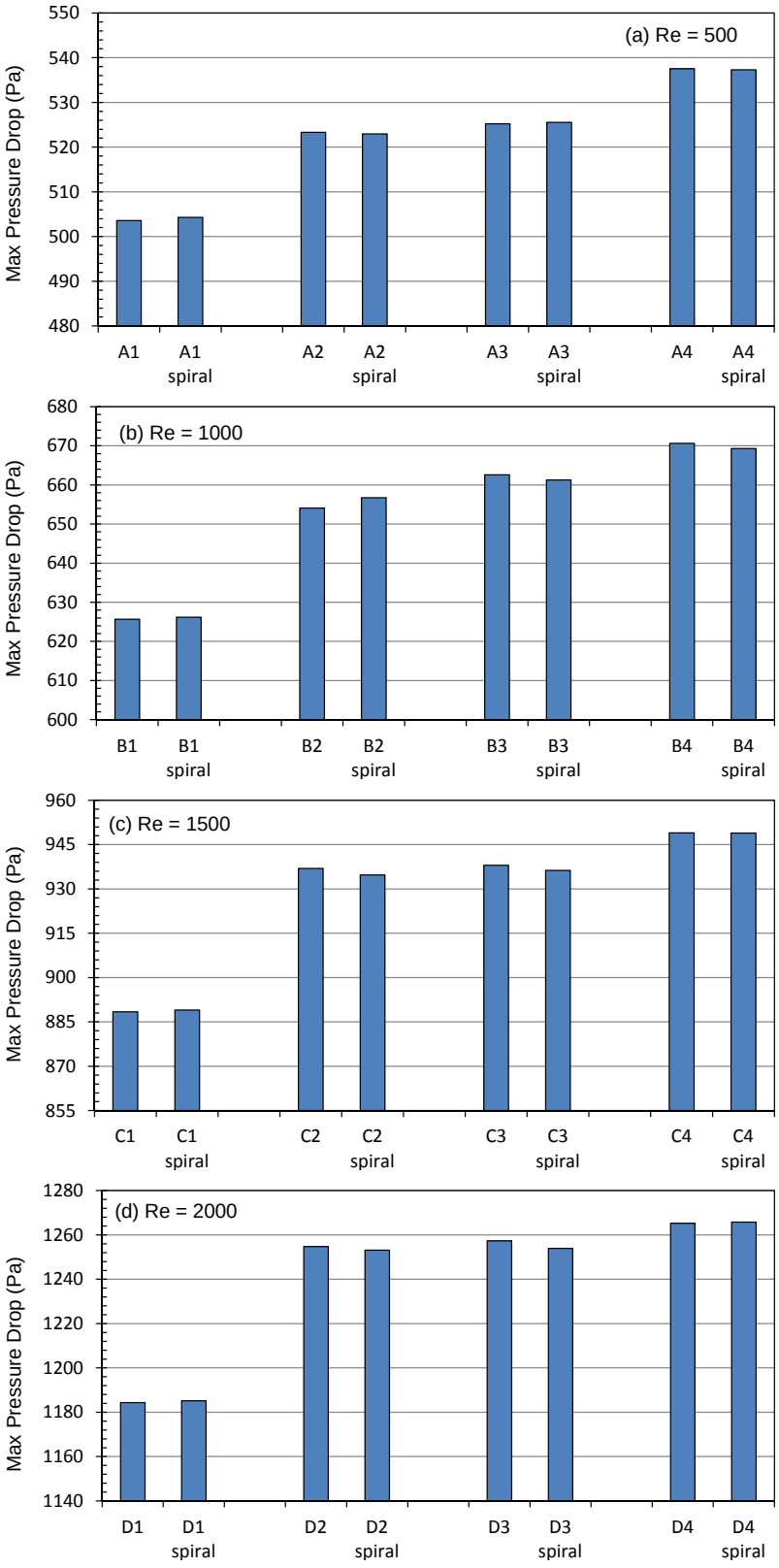


Figure 22: Bar charts of the maximum blood pressure drop for both the non-spiral and spiral flow in all models for (a) $Re = 500$, (b) $Re = 1000$, (c) $Re = 1500$ and (d) 2000.

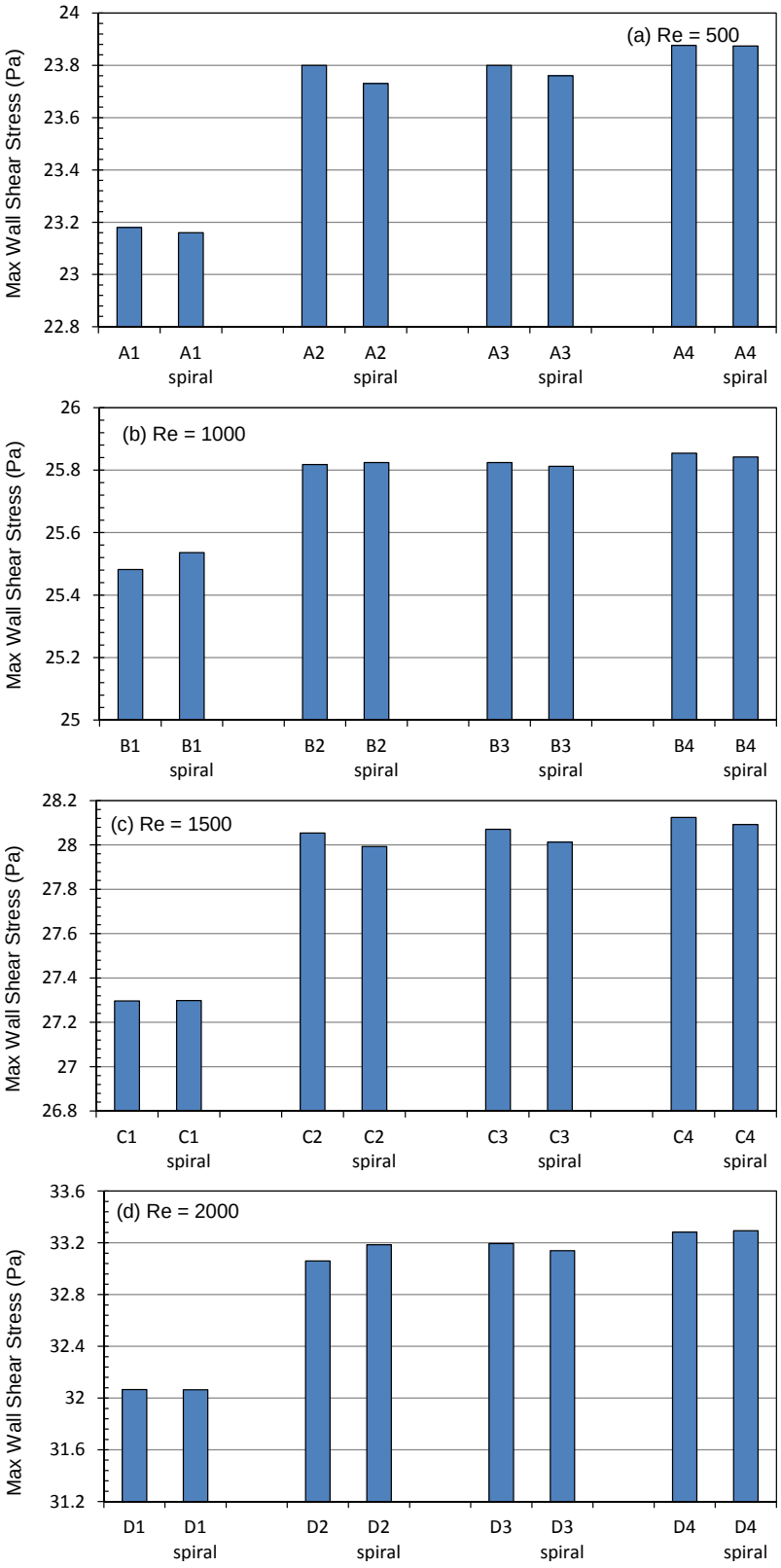


Figure 23: Bar charts of the maximum wall shear stress for both the non-spiral and spiral flow in all models for (a) $Re = 500$, (b) $Re = 1000$, (c) $Re = 1500$ and (d) 2000.